

Foreword

This work, performed with the support of the SRF materials R&D group of the Fermilab Technical Division (Batavia, IL – U.S.), addresses the investigation of the physics underlying the chemical etching process (i.e. BCP – Buffered Chemical Polishing) of superconducting RF elliptical cavities.

High purity is a key requirement of the Niobium used for fabrication of superconducting RF cavities, which are the core component of the International Linear Collider.

For this reason, the cavities undergo a series of treatments aimed at removing any form of contamination in their superficial layer. BCP is a basic step of strong relevance in the processing sequence. This technique has proven to be simple and economical, while guaranteeing reliable results with very high reproducibility of cavity performances. Nevertheless it is also proven to be the step limiting the accelerating gradient below 30 MV/m in cavities made out of polycrystalline material. This limit can be overcome if large grain or single crystal material becomes available and the technological issues of fabricating cavities out of this material are solved. The combination of BCP and single crystal material would result in a large cost saving for large projects such as ILC since it would reduce both the costs of material and of its processing.

Wishing that BCP may become the reference technique for treating high gradient superconducting resonant cavities, this dissertation analyzes the physical aspects involved in the BCP and aim to the optimization of the process itself.

The investigation of the phenomenon has been formalized by means of numerical modeling using a finite element commercial code.

The work hereafter does not claim to be a full explanation of the complex physics of the BCP process, but certainly surfaced a number of aspects that can be very useful for both the optimization of the cavity processing and the design of new facilities.

1. THE INTERNATIONAL LINEAR COLLIDER (ILC)

1 Introduction

The work described in this thesis regards the construction of the ILC. Given that the proposed construction of the ILC is motivated by physics research it is deemed pertinent that these motivations be mentioned. This introduction is therefore devoted in part to a brief summary of the current state of this physics research, beginning with an overall view and following up with the details which motivate the ILC.

1.1 The big picture

Elementary particle physics has the ambitious goal of explaining the innermost building blocks of matter and the fundamental forces acting between them. Starting with the discovery of the electron, particle physicists have ventured progressively deeper into the unseen world within the atom. Their discoveries have redefined the human conception of the physical world, connecting the smallest elements of the universe to the largest, and to the earliest moments of its birth.

The masses of particles and the strength of the forces have played a key role in the evolution of the universe from the Big Bang to its present appearance in terms of galaxies, stars, black holes, chemical elements and biological systems. Discoveries in particle physics thus go to the very core of our existence.

As a consequence of the interplay of theory and experiment, in which the evolution of accelerators has played a key role, particle physics has made enormous progress in the course of the last century. The current view is that nature is composed of two basic sets of fundamental particles: the quarks and leptons (among the leptons are electrons and neutrinos), and a set of fundamental forces that allow these to interact with each other. The "forces" themselves can be regarded as being transmitted through the exchange of particles called gauge bosons. An example of these is the photon, the quantum of light and the transmitter of the electromagnetic force we experience every day. This view is formalized by the Standard Model. The Standard Model is one of the most consistent formulations and probably the most elegant theory in the field of physics [1].

Nevertheless, the Standard Model theory is only an intermediate step in the formulation of a more complete theory, which will include the gravitational force. It is believed by many physicists that the four main forces present in nature (electromagnetic force, weak force, strong force and gravitational force) can be unified into one fundamental force at very high energies.

The most popular theory, which could supersede the Standard model, is Supersymmetry which in fact predicts that, at the extreme energies which were present just after the Big Bang, all of nature's forces were combined in one single

force[2]. These split into the four forces that we know today as the universe cooled.

Our current understanding is the fruit of enormous intellectual and economic expenditure involving the whole scientific community working in diverse projects. Prominent amongst these are the high energy accelerators which reach for progressively higher energies. New technologies and materials must be developed in order to reach these higher energies and it is at this point that physicists and engineers find common ground.

The contributions of present accelerators like LEP at CERN and the Tevatron at Fermilab set the scene for the most recent and largest of these accelerators, the LHC which is about to begin taking data at CERN and for the proposed construction of the ILC. A little further detail is needed to explain this progression.

1.2 The Standard Model and beyond

Nowhere have the predictions of the Standard Model found more convincing corroboration than in its ability to explain the results of collisions between the high energy protons and antiprotons or electrons and positrons accelerated and made to collide by means of accelerators. In the past thirty years, huge strides were made in understanding the interrelationships of the strong force that binds the nuclei, the electromagnetic force, and the weak force that causes radioactive decays and powers the sun.

All the three forces are now understood in terms of ‘gauge theories’ in which the symmetry of fields dictates the existence of force-carrying particles (the gauge bosons) that have one unit of spin and no mass. The forces are exerted upon the quarks and leptons, the building blocks of matter, through gauge boson exchanges. The strong force is mediated by a set of eight gluons, and the electromagnetic force by the photon. The weak force requires quite massive force carriers called the W and Z bosons to account for its short range. The three forces are distinguished by characteristic particle properties such as electric charge, to which each of the forces respond. Though the electromagnetic and weak forces seem quite different in the laboratory experiments, it is understood now that they are in fact two aspects of a unified whole.

These ideas form the basis for the standard model, whose predictions have now been confirmed through hundreds of experimental measurements. Experiments over the past two decades using accelerators at CERN, SLAC and Fermilab discovered the W and Z bosons, demonstrated their close connection to the photon, and firmly established the unified electroweak interaction. The puzzle of the massive W and Z bosons is explained in terms of primordial weak and electromagnetic force carriers were originally mass-less, but acquire mass through an electroweak symmetry breaking mechanism. The standard model hypothesizes is that this mechanism is associated with a Higgs boson, so far undetected. This standard model Higgs boson should be discovered in experiments at sufficiently large collision energy. Although it has yet to be observed, the standard model predicts its properties precisely, its spin and internal quantum numbers; its decays to quarks, leptons, or gauge bosons; and its self-interaction. Only the Higgs boson’s mass is not specified by the theory.

Over the years the wealth of high precision studies of W, Z and photon properties, the direct observation of the massive top quark, and neutrino scattering rates have confirmed the validity of the standard model and have severely constrained possible alternatives. These studies give a range within which the Higgs boson mass should lie. From the direct searches, it is known that the Higgs boson mass is larger than about 114 GeV. The precision measurements limit the Higgs mass to less than about 200 GeV in the context of the standard model, and only somewhat larger for allowed variant models. The most likely Higgs mass is in fact just above the present experimental lower mass limit.

The proton-antiproton Tevatron Collider now operating at Fermilab could discover some of the lower mass states involved in electroweak symmetry breaking. In 2007, the LHC now under construction at CERN will obtain its first proton collisions at 14 TeV and it is therefore expected to discover a standard model Higgs boson over the full potential mass range. It should also be sensitive to new physics into the several TeV range.

The program for the future International Linear Collider (ILC) will be set in the context of the discoveries made at the LHC. However it is certain that, whatever the scenario, a detailed understanding of the results produced by the LHC will require a precision high energy electron – positron collider like the ILC [1].

1.3 Understanding the Higgs boson

The prime goal for the next round of experiments is finding the agent that gives mass to the gauge bosons, quarks and leptons. This quest offers an excellent illustration of how the LHC and the e^-e^+ (electron-positron) International Linear Collider will magnify each other's power. If the answer is the standard model Higgs boson, the LHC will see it. However, the backgrounds to the Higgs production process at the LHC are large, making the measurements of the couplings to quarks, quantum numbers, or Higgs self-couplings difficult. Having learnt where to look for it from the LHC, the ILC can make the Higgs boson with little background, producing it in association with only one or two additional particles, and can therefore measure the Higgs properties much more accurately.

Even if it decays into invisible particles, the Higgs can be easily seen and studied at the ILC through its recoil from a visible Z boson [1].

The precision measurements at the ILC are crucial to reveal the character of the Higgs boson. If the symmetry of the electroweak interaction is broken in a more complicated way than foreseen in the standard model, these same precision measurements, together with new very precise studies of the W and Z bosons and the top quark are only possible at a machine like the ILC and they will strongly constrain whatever picture corresponds to reality.

1.4 Particle Accelerators

The particle accelerator has played a key role in the evolution of nuclear and elementary particle physics. The underlying principle is very simple: charged ions or electrons are accelerated to very high velocities and made to collide with atoms contained in a stationary target or with another beam of charged particles traveling

in the opposite direction. The kinetic energies imparted to the charged particles by the accelerator are large enough to fragment the particles into their constituents.

The accelerator is therefore an indispensable tool in this kind of research. Other tools are required to observe and characterize the products of the collision. These tools make up what is comprehensively known as the “detector” which is situated close to the point where the impact takes place. The most energetic collisions take place when beams traveling in opposite directions are made to collide head – on and the collider detectors which surround the impact point are giant systems composed by different types of detectors (calorimeters, scintillators, gas chambers) which are disposed in layers with the classical “onion” structure. The detector has the fundamental task of identifying the types and characteristics (e.g. the mass) of the particles generated by the impact from simultaneous measurements of energy and momentum. To this end, a combination of different detectors disposed all around the center of impact is necessary.

The following *Figure 1.1* illustrates schematically the structure of a typical detector.

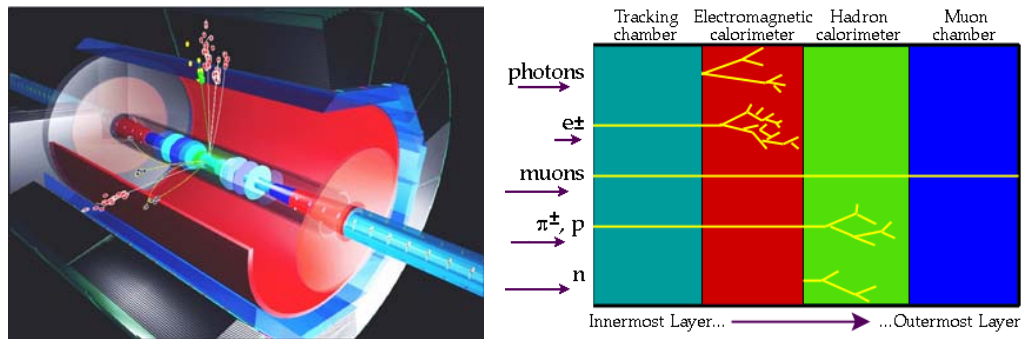


Fig. 1.1 Schematic of a typical detector.

From the very beginning, accelerator development has followed two distinct paths: circular acceleration, beginning with Lawrence’s cyclotron in 1931 and linear acceleration beginning with the Vandegraaf around the same period and the Cockcroft-Walton shortly thereafter. Early linear accelerators relied on electrostatic acceleration of charged ions by means of static field whereas the cyclotron applied electrostatic fields at frequencies corresponding to the circulating ions (i.e. at radiofrequencies) to impart an acceleration at each turn.

With time and the need of ever higher energies, cyclotrons gave way to synchrotrons of ever increasing radius while linear RF accelerators were developed. For reasons outlined below, the highest energies are reached by synchrotrons when they are used to accelerate protons (or antiprotons). Because of the higher energies, these machines have a greater potential for discovery so that most important discoveries have been made employing circular synchrotrons, e.g. the discovery of the sixth and heaviest quark (the top quark) using the TEVATRON accelerator at Fermilab. This was the first synchrotron accelerator made with superconducting magnets and able to accelerate protons and antiprotons to an energy of 980 GeV, corresponding to a total center – of – mass energy of ~ 2 TeV in a collision between protons and antiprotons traveling in opposite directions. However, these machines have the disadvantage of producing a large quantity of unwanted particles (generally termed “background”), in

addition to those of interest, because the colliding protons and antiprotons are themselves composed by more elementary particles (gluons and quarks) and because these particles interact by means of the “strong” nuclear force which is capable of generating many other fundamental particles.

On the other hand, since the electron is itself an elementary particle and it interacts by means of the weaker electromagnetic force, collisions between electrons and positrons are much cleaner. Electron-positron colliders therefore yield cleaner and more precise information but, being electrons much lighter, the radiation emission of an electron accelerated in a circular trajectory leads to much higher energy losses in synchrotrons (synchrotron radiation emission). These losses impose severe lower limits to the radius of curvature and the best way to obtain high kinetic energies is to accelerate the electron along a straight trajectory by means of a radio frequency (RF) linear accelerator.

The basic principles underlying these two strategies to achieve particle acceleration are outlined in the following sections.

1.4.1 Synchrotron

The particles are constrained in a vacuum pipe bent into a torus, which threads a series of electromagnets, providing a field normal to the plane of the orbit. For a proton of momentum p in GeV/c and a given bending radius ρ , the field provided by the dipole magnets must have a value of B (in Tesla), where:

$$p = 0.3 \cdot B \cdot \rho \quad (1.1)$$

The particles are accelerated once or more times per revolution by RF cavities. Both the field B and the RF frequency must increase and be synchronized with the particle velocity as it increases -hence the term of synchrotron-. Protons are usually injected from a linac source at low energy and at low field B , which increase to its maximum value over the accelerating cycle, typically lasting for a few seconds. Then the cycle begins again.

As mentioned above, the energy obtained with the proton synchrotron is determined by the ring radius and the maximum value of B . For conventional electromagnets using copper coils, B_{\max} is in the order of 1.4 T, while, if superconducting coils are used, fields of 10T or more are possible. As an example the Fermilab TEVATON synchrotron (*Fig. 1.2*) is 1 Km in radius and it achieved an energy of 400 GeV with conventional magnets while now, using superconducting magnets, it consistently runs at 1000GeV (1TeV).



Fig. 1.2 Fermilab Acceleration Complex.

1.4.2 Linear Accelerators

The simplest accelerator is the cathodic tube of a common television. In this case the electrons are generated by a hot filament and then accelerated by the difference of potential between two charged plates (the anode and the cathode). More sophisticated electrostatic accelerators are the Vandegraaf and the Cockroft-Walton mentioned above but the ultimate limitation of these types of accelerators arises from the maximum practical potential difference that can be held by the charged surfaces without electric discharge. Another strategy must be used to reach higher energies. The best way so far achieved to obtain this purpose is the employment of a RF linear accelerator.

RF linear accelerators are divided in two types:

- RF drift tube accelerators
- RF cavity accelerators.

The drift tube linear accelerators consist of an evacuated pipe containing a set of metal drift tubes, with alternate tubes attached to either side of the radiofrequency voltage. The ion source is continuous, but only those bunches of ions inside a certain time interval will be accelerated. Such ions cross the gap between successive tubes (*Fig. 1.3*) when the field is from left to right, and are inside a tube (therefore in a field free region) when the voltage change sign.

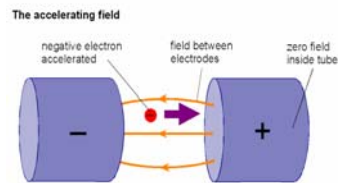


Fig. 1.3 Drift tube acceleration scheme.

If the increase in length of each tube along the accelerator is correctly chosen, as the ion velocity increases under acceleration, the ion in a bunch receive a continuous acceleration (*Fig. 1.4*).

Typical fields obtained with such technique are a few MeV per meter of length. Such proton linacs, reaching energies in the order of 50MeV, are used as injectors for the later stages of cyclic accelerators.

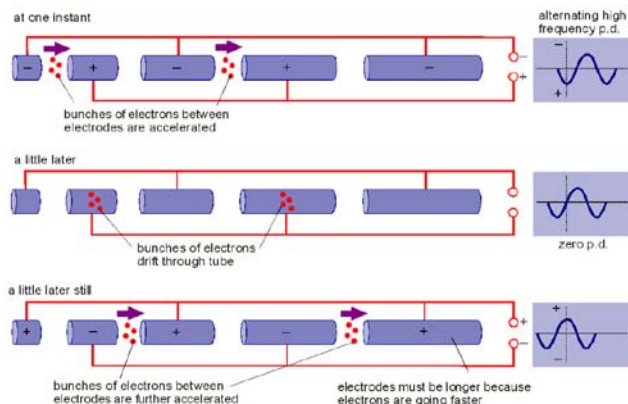


Fig. 1.4 Schematic of a drift tube accelerator.

Electrons above a few MeV energy travel essentially with the velocity of light, so that after the first meter or so, an electron linac has tubes of uniform length. In practice, frequencies in the microwave range are employed and the tubes are resonant cavities of a few centimeters in dimension fed by a series of Klystron oscillators (A Klystron is a power amplifier that supplies power for the high-energy end of LINAC), which are synchronized in time to provide continuous acceleration.

After your description of Drift tube linacs, a brief but generic introduction to rf cavity linacs would be suitable here before you turn to the specifics of the ILC.

1.5 ILC Layout

The overall layout of the ILC is shown in the following *Figure 1.5*.

Its total length on the main linac is expected to be about 33 km depending on the achievable average gradient of the cavities [1]. The main components are a pair of linear accelerators, one for electrons and one for positrons, pointing at each other. Each linear accelerator is constructed from about 16,000 one-meter long superconducting cavities, made in niobium and cooled by superfluid helium at -271 C. Pulsed radio frequency (1.3Ghz) electromagnetic fields are guided at 5 Hz for the duration of one millisecond into the cavities to accelerate the particles.

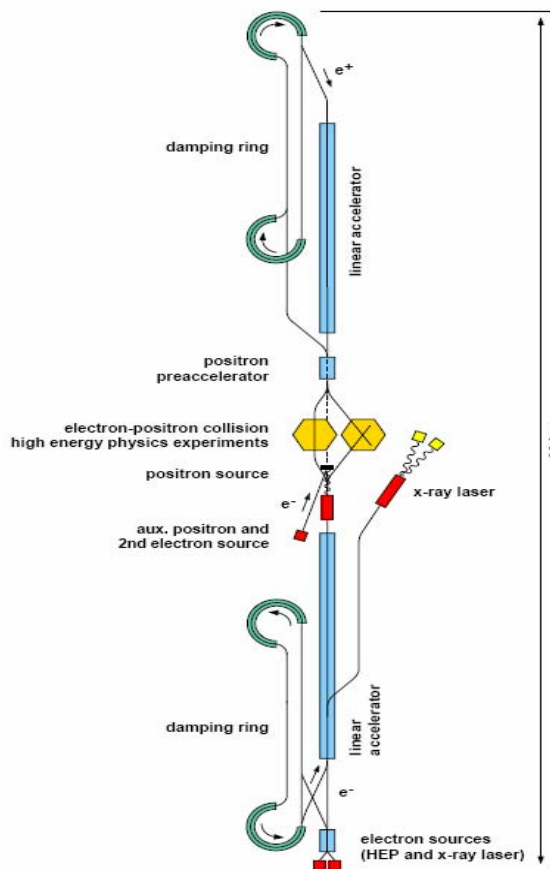


Fig. 1.5 Proposed ILC layout.

Superconducting technology provides important advantages for an accelerator in general. As the power dissipation in the cavity walls is extremely small, the power transfer efficiency from the RF source to the particles is very high, thus keeping the electrical power consumption within acceptable limits (circa 100MW), even for a high average beam power. The high beam power is an essential requirement to obtain a high rate of electron-positron collisions.

The electron beam for the collider is generated by a polarized laser driven source. After a short section of conventional (not superconducting) linear accelerator, the beam is accelerated to 5 GeV in superconducting structures identical to the ones used for main accelerator.

The electrons are stored in a damping ring at 5 GeV to reduce the beam size down to values needed for high luminosity operation. As the train of bunches is really long, a compression scheme is used to store the bunches in the damping ring. One of the options presently under investigation is the use of the so-called dog bone design with two 8 km straight sections, where most of the length can be accommodated inside the main accelerator tunnel. Only two 1km loops are needed at either end. After damping, the bunch train is decompressed and injected into the main linear accelerator.

A conventional positron source cannot provide the total charge of about $5 \cdot 10^{13}$ positrons per beam pulse needed for the high luminosity operation of the collider. Therefore an alternative technique has to be adopted such as the following: an intense photon beam is generated by passing the high energy electron beam through an undulator magnet placed after the main linear accelerator. Positrons are produced by directing the photons onto a thin target in which they are converted into pairs of electrons and positrons. After acceleration to 250 MeV in a normal conducting linear accelerator the positron beam is transported to a 5 GeV superconducting accelerator and injected into the positron damping ring.

The RF power to excite the superconducting cavities is generated by ~300 klystrons per linear accelerator [1].

The two linear accelerators will be installed in an underground tunnel of 5.2 m diameter (Fig. 1.6).

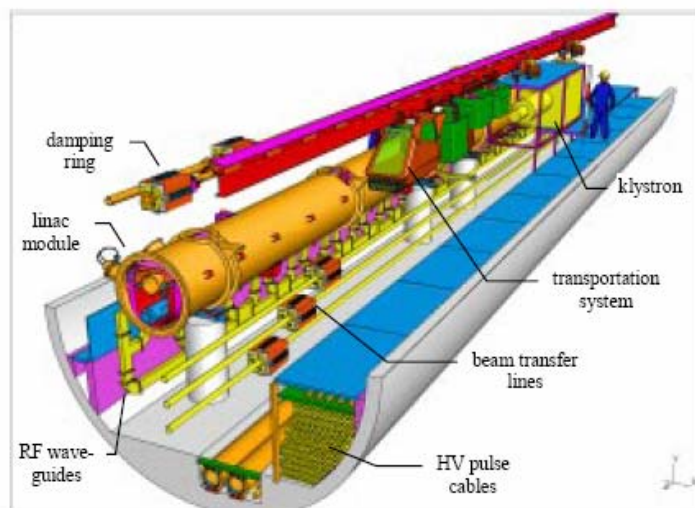


Fig. 1.6 Proposed ILC Tunnel View.

2 NUMERICAL ANALYSIS

2 Introduction

Finding the exact solution of partial different equations is possible only in few situations characterized by simple geometries and boundary conditions. In all the other cases it is only possible to obtain and approximate solution by means of numerical techniques, such as finite elements of finite differences methods.

Thanks to the development of computers and the progressive increase of their computing power, nowadays computational simulations allow one to reach extremely accurate solutions using numerical techniques [3].

A complete description and discussion of these methods is outside the scope of this thesis. This chapter will concentrate exclusively on the specific techniques adopted for the simulations performed in this work

2.1 Equations Governing the BCP Process

The equations used to describe the BCP process are:

- Momentum conservation equations.

The differential form of the Navier-Stokes equations for incompressible fluids is the following:

$$\rho \frac{\partial u}{\partial \theta} + \rho \left(u \frac{\partial u}{\partial x} + v \frac{\partial u}{\partial y} + w \frac{\partial u}{\partial z} \right) = \mu \left(\frac{\partial^2 u}{\partial x^2} + \frac{\partial^2 u}{\partial y^2} + \frac{\partial^2 u}{\partial z^2} \right) - \frac{\partial P}{\partial x} \quad \text{x-component (2.1)}$$

$$\rho \frac{\partial v}{\partial \theta} + \rho \left(u \frac{\partial v}{\partial x} + v \frac{\partial v}{\partial y} + w \frac{\partial v}{\partial z} \right) = \mu \left(\frac{\partial^2 v}{\partial x^2} + \frac{\partial^2 v}{\partial y^2} + \frac{\partial^2 v}{\partial z^2} \right) - \frac{\partial P}{\partial y} \quad \text{y-component (2.2)}$$

$$\rho \frac{\partial w}{\partial \theta} + \rho \left(u \frac{\partial w}{\partial x} + v \frac{\partial w}{\partial y} + w \frac{\partial w}{\partial z} \right) = \mu \left(\frac{\partial^2 w}{\partial x^2} + \frac{\partial^2 w}{\partial y^2} + \frac{\partial^2 w}{\partial z^2} \right) - \frac{\partial P}{\partial z} \quad \text{z-component (2.3)}$$

where ρ is the fluid density, μ is the fluid viscosity, θ is the temporal variable and P is the pressure

This system of equations describes the velocity field $\underline{v} = (u, v, w)$ within the space domain $\Omega = (x, y, z)$.

- Energy Equation (convection and conduction):

$$\rho c_p \frac{\partial t}{\partial \theta} + \rho c_p \left(u \frac{\partial t}{\partial x} + v \frac{\partial t}{\partial y} + w \frac{\partial t}{\partial z} \right) = \lambda \left(\frac{\partial^2 t}{\partial x^2} + \frac{\partial^2 t}{\partial y^2} + \frac{\partial^2 t}{\partial z^2} \right) + H \quad (2.4)$$

where:

c_p is the specific heat, λ the conductivity coefficient and H is the internal heat generation term.

The solution of this equation describes the distribution of the temperature field $t(x,y,z)$ inside the domain $\Omega = (x, y, z)$.

– Chemical Equation (convection and diffusion)

$$\frac{\partial c}{\partial t} + \left(u \frac{\partial c}{\partial x} + v \frac{\partial c}{\partial y} + w \frac{\partial c}{\partial z} \right) = D \left(\frac{\partial^2 c}{\partial x^2} + \frac{\partial^2 c}{\partial y^2} + \frac{\partial^2 c}{\partial z^2} \right) + R \quad (2.5)$$

where:

$c(x,y,z)$ is the concentration of a given chemical specie inside the domain $\Omega = (x,y,z)$,

D is the diffusivity coefficient and R is the reaction rate.

The solution of this equation describes the concentration of a chemical specie inside the domain $\Omega = (x,y,z)$.

2.2 Generalization of the Partial Differential Equation

One observes a pronounced similarity between the fluid dynamic, thermal and chemical equations. A partial differential equation in the unknown (scalar) function $\Phi = \Phi(\xi, \eta)$ can be in fact expressed in its more generic form:

$$A \frac{\partial^2 \Phi}{\partial \xi^2} + B \frac{\partial^2 \Phi}{\partial \xi \partial \eta} + C \frac{\partial^2 \Phi}{\partial \eta^2} + D \frac{\partial \Phi}{\partial \xi} + E \frac{\partial \Phi}{\partial \eta} + F \Phi + G = 0 \quad (2.6)$$

If the coefficients A, B, C, D, E, F and G do not depend on Φ the partial differential equation is linear (conversely it is Non-linear) the term

$$B^2 - 4AC \quad (2.7)$$

defines the type of differential equation:

$$B^2 - 4AC < 0$$

the equation is elliptical and describes a stationary regime;

$$B^2 - 4AC = 0$$

the equation is parabolic and describes a time dependent diffusion process, such as heat propagation;

$$B^2 - 4AC > 0$$

the equation is hyperbolic and describes directional propagation (wave like) with finite velocity.

For example, the elliptic equation in a bi-dimensional domain

$$\lambda \frac{\partial^2 t}{\partial x^2} + \lambda \frac{\partial^2 t}{\partial y^2} = 0 \quad (2.8)$$

Describes the conduction stationary regime. With respect to the 2.6 $A = \lambda$, $B = 0$ and $C = \lambda$, then $B^2 - 4AC < 0$.

The same physical phenomenon in a mono-dimensional domain and in the transient regime is described by:

$$\rho c \frac{\partial t}{\partial g} - \lambda \frac{\partial^2 t}{\partial x^2} = 0 \quad (2.9)$$

With respect to 2.6 $A = 0$, $B = 0$ and $C = \lambda$, hence $B^2 - 4AC = 0$ and the equation is parabolic.

The character of the equation (elliptic, parabolic or hyperbolic) describing the process has a deep influence in the strategy used for its resolution. The parabolic or hyperbolic equations can in fact be solved by reducing them to a sequence of elliptic equations by applying a time marching method.

This method consists in discretizing the time period of interest in short steps and evaluating the numerical solution at each time step as though it were stationary. Previous time steps enter into the equation defining the current solution as “forcing terms”.

2.3 Boundary conditions:

In order to solve a partial differential equation within a domain $\Omega = (x, y)$, it is necessary to consider the boundary conditions that characterize the problem.

There are three basic types of boundary conditions:

- Dirichlet condition
- Neumann condition
- Robin condition

2.3.1 First type: Dirichlet condition

This is the case when the value of a variable is defined on the boundary $\partial\Omega$ of the domain :

$$\Phi = f_1(\underline{x}) \quad \underline{x} = (x, y) \in \partial\Omega \quad (2.10)$$

In the thermal-fluid case this condition is used to fixing the velocity field or the temperature on a part of the boundary domain.

2.3.2 Second type: Neumann condition

$$\frac{\partial \Phi}{\partial n} = f_a(\underline{x}) \quad \text{where} \quad \frac{\partial \Phi}{\partial n} = \nabla \Phi \cdot \underline{n} = \left(\frac{\partial \Phi}{\partial x} \underline{i} + \frac{\partial \Phi}{\partial y} \underline{j} \right) \cdot (n_x \underline{i} + n_y \underline{j}) \quad (2.11)$$

where:

∇ is the gradient differential operator, \underline{i} and \underline{j} are the unitary base vectors of the reference system, and $\underline{n} = (n_x \underline{i} + n_y \underline{j})$ is the outward pointing vector in a given boundary point.

In a thermal-fluid dynamic case, this condition can describe a symmetry (no mass flux throughout a part of boundary) or an imposed thermal flux.

2.3.3 Third type: Robin condition

The Robin condition is a combination of the two previous boundary conditions:

$$a(\underline{x})\Phi + b(\underline{x})\frac{\partial\Phi}{\partial n} = f_3(\underline{x}) \quad (2.12)$$

In a thermal model this condition can describe the convective flux.

2.4 Finite Differences approach

The concept of discretization of the physical domain is fundamental in the development of numerical methods. This procedure consists in defining a fine grid (or mesh) of points called nodes (In figure 2.1 is shown a mono dimensional mesh where the nodes are separated by a Δx spacing).

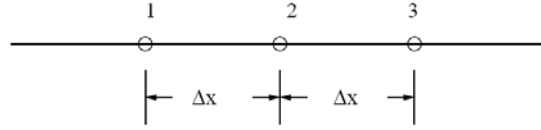


Fig. 2.1 One dimensional mesh

The differential operators in the PDE are then replaced by difference operators and the solution is computed only in the nodes of the domain.

This method transforms the differential system into an algebraic one, whose numerical solution yields an approximation of the exact solution values in the mesh points.

A brief review of the finite difference method is fundamental for a better understanding of the finite element method. The mostly used difference operators used that replace the differential operators are listed below:

$$\left(\frac{d\Phi}{dx}\right)_j \cong \frac{\Phi_j - \Phi_{j-1}}{\Delta x} \quad \text{backward difference operator (2.13)}$$

$$\left(\frac{d\Phi}{dx}\right)_j \cong \frac{\Phi_{j+1} - \Phi_j}{\Delta x} \quad \text{forward difference operator (2.14)}$$

$$\left(\frac{d\Phi}{dx}\right)_j \cong \frac{\Phi_{j+1} - \Phi_{j-1}}{2\Delta x} \quad \text{central difference operator (2.15)}$$

$$\begin{aligned} \left(\frac{d^2\Phi}{dx^2}\right)_j &= \left[\frac{d}{dx}\left(\frac{d\Phi}{dx}\right)\right]_j \cong \left[\frac{\Delta}{\Delta x}\left(\frac{\Delta\Phi}{\Delta x}\right)\right]_j = \frac{1}{\Delta x} \left[\frac{\Phi_{j+1} - \Phi_j}{\Delta x} - \frac{\Phi_j - \Phi_{j-1}}{\Delta x} \right] = \\ &= \frac{\Phi_{j+1} - 2\Phi_j + \Phi_{j-1}}{(\Delta x)^2} \quad \text{second order central difference operator (2.16)} \end{aligned}$$

2.4.1 Finite Differences time dependent study

In a generic partial differential equation, the temporal variable is responsible for its parabolic behavior. With reference to section 2.2, it is considered the equation

$$\rho c \frac{\partial t}{\partial \vartheta} = \lambda \frac{\partial^2 t}{\partial x^2} \Rightarrow \frac{\partial t}{\partial \vartheta} = a \frac{\partial^2 t}{\partial x^2} \quad (2.17)$$

where $a = \frac{\lambda}{\rho c}$ is the diffusivity coefficient

Since the time variable appears in the equation, a time-marching technique should be used to describe the evolution of the unknown variable in time. There are two classical methods used to solve the time dependent problems: explicit and implicit.

2.4.1.1 Explicit method

The time derivative operator is replaced by the forward difference operator, and the equation assume the follow form:

$$\frac{t_j^{n+1} - t_j^n}{\Delta \vartheta} = a \frac{t_{j+1}^n - 2t_j^n + t_{j-1}^n}{\Delta x^2} \quad (2.18)$$

Since this equation presents only one unknown variable, the solution can be obtained explicitly.

The main issue with this method is its stability during the time marching process. In fact if the time step is not small enough, wild oscillations appear in the computed solution.

For the conductive-convective case, the oscillations obtained during computation are avoided if:

$$Fo_{\Delta} = \frac{a \Delta \vartheta}{\Delta x^2} \leq \frac{1}{2(Bi_{\Delta} + 1)} \quad (2.19)$$

where Fo_{Δ} is the cell Fourier number and $Bi_{\Delta} = \frac{\alpha \Delta x}{\lambda}$ is the Biot number.

In the case of simple conduction, the stability condition is

$$Fo_{\Delta} = \frac{a \Delta \vartheta}{\Delta x^2} \leq \frac{1}{2} \quad (2.20)$$

2.4.1.2 Inverse method

The time derivative operator is replaced by the backward difference operator, and the equation assume the follow form:

$$\frac{t_j^{n+1} - t_j^n}{\Delta \vartheta} = a \frac{t_{j+1}^{n+1} - 2t_j^{n+1} + t_{j-1}^{n+1}}{\Delta x^2} \quad (2.21)$$

In this case a linear system of equations with three unknown for each equation must be solved. This approach doesn't require any additional stability conditions to be applied

2.5 Finite Elements Method (FEM)

This method, unlike the finite differences method, allows to obtain an approximate solution of the problem in the entire domain of the model.

In this case the domain is divided in a number of parts calling mesh elements and the approximate unknown Φ^* is computed at the vertex of the elements.

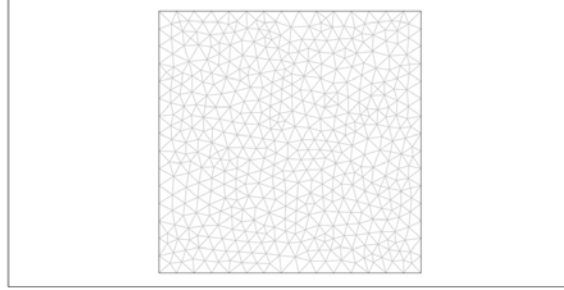


Fig. 2.2 Triangular bi dimensional mesh (from COMSOL)

Suitable shape functions are used to interpolate the solution within the elements themselves.

For example a generic variable is approximated in a one-dimensional domain as follows:

$$\Phi(x) \cong \Phi^*(x) = \sum_{i=1}^n N_i(x) \Phi_i \quad (2.22)$$

when adopting a global numeration for the nodes (in the global reference all n nodes of the discretization are considered)

$$\text{or } \Phi(x) \cong \Phi^*(x) = \sum_{e=1}^m \sum_{i=1}^r N_i^e(x) \Phi_i^e \quad (2.23)$$

when considering the single element e (the single element defines a local reference of r nodes) and defining the whole domain as the sum of the m single elements that constitute the mesh.

In the above equation $N_i(x)$ is the shape function used to represent the unknown variable within the element. The shape function satisfies the following conditions:

- 1- Since the unknown function doesn't depend upon the independent variable x ,

$$\Phi(x_i) \cong \Phi^*(x_i) = \Phi_i \quad (2.24)$$

The shape function must fulfill

$$\begin{aligned} N_i^e(x_i^e) &= 0 \text{ if } i \neq j \\ N_i^e(x_i^e) &= 1 \text{ otherwise} \end{aligned} \quad (2.25)$$

2- To describe the constant case, the shape function must fulfill also the following condition:

$$\Phi^e(x) = \text{const.} = \Phi^e = \sum_{i=1}^r N_i^e(x) \Phi^e \quad (2.26)$$

which implies

$$\sum_{i=1}^r N_i^e = 1 \text{ independently on } x \quad (2.27)$$

2.5.1 Weighted Residual version

Equation 2.6), can be also represented in more compact notation as

$$F(\Phi) = 0 \quad (2.28)$$

If the unknown variable is substituted by its approximation the starting above equation is no longer satisfied , since in general

$$F(\Phi^*) = \varepsilon \neq 0 \quad (2.29)$$

A finite elements method is obtained by imposing that the residual ε be orthogonal to a suitable number of weight functions W_i . This number must be equal to the n degrees of freedom of the approximation sought.

$$\int_{\Omega} W_i A(t^*) d\Omega = 0 \quad i=1 \dots n \quad (2.30)$$

The weight functions have the same properties as the shape functions.

The stationary conduction equation in a bi-dimensional domain $\Omega(x, y)$ is used as an example to explain the weighted residual method as in the case of the finite differences method.

The conduction equation can be written in its compact form as follows:

$$A(t) = \nabla \cdot (\lambda \nabla t) + H = 0 \quad (2.31)$$

When the weighted residual method is applied, the system of n equations

$$\int_{\Omega} W_i (\nabla \cdot (\lambda \nabla t)) d\Omega + \int_{\Omega} W_i H = 0 \quad i=1 \dots n \quad (2.33)$$

Is not well defined since the term $\nabla \cdot (\lambda \nabla t)$ contains a second order derivative and the shape functions that appear in the approximate representation of the unknown variable are not twice differentiable.

In order to overcome this problem, the Gauss Green formula, shown below, is adopted to reduce the equation by one order.

$$\int_{\Omega} \nabla \underline{V} = \int_{\Omega} \underline{V} \cdot \underline{n} \, ds \text{ where } \underline{V} \text{ is a generic vectorial field} \quad (2.34)$$

By defining $W_i(\lambda \nabla t) = \underline{V}$ and applying gauss green with simple operations, one obtains

$$\int_{\Omega} \nabla \cdot (W_i \lambda \nabla t) d\Omega = \int_{\Omega} \nabla W_i \cdot (\lambda \nabla t) d\Omega + \int_{\Omega} W_i \nabla \cdot (\lambda \nabla t) d\Omega = \int_{\partial\Omega} (W_i \lambda \nabla t) \cdot \underline{n} \, dS \quad (2.35)$$

$$\Rightarrow \int_{\Omega} W_i \nabla \cdot (\lambda \nabla t) d\Omega = \int_{\partial\Omega} (W_i \lambda \nabla t) \cdot \underline{n} \, dS - \int_{\Omega} \nabla W_i \cdot (\lambda \nabla t) d\Omega \quad (2.36)$$

And the second derivatives disappear. Hence, the system of equations is well defined and assume the following form:

$$-\int_{\Omega} \nabla W_i \cdot (\lambda \nabla t) d\Omega - \int_{\partial\Omega} W_i \underline{q} \cdot \underline{n} \, dS + \int_{\Omega} W_i H \, d\Omega = 0 \quad (2.37)$$

where, in the specific case, $\lambda \nabla t = -\underline{q}$ is the Fourier term of conduction flux throughout the boundary.

2.5.2 Galerkin version:

Since both the shape functions and the weight functions satisfy the same requirements, in the Galerkin finite element version the weight functions are equal to the shape functions.

The conduction equation solved by Galerkin become:

$$\frac{\partial}{\partial x} \left(\lambda \frac{\partial t}{\partial x} \right) + \frac{\partial}{\partial y} \left(\lambda \frac{\partial t}{\partial y} \right) + H = 0 \quad (2.38)$$

$$\int_{\Omega} N_i \left[\frac{\partial}{\partial x} \left(\lambda \frac{\partial t}{\partial x} \right) + \frac{\partial}{\partial y} \left(\lambda \frac{\partial t}{\partial y} \right) + H \right] d\Omega = 0 \quad (2.39)$$

When the Gauss Green formula is applied and the approximate representation of the unknown variable t is introduced, the system becomes:

$$-\int_{\Omega} \left[\frac{\partial N_i}{\partial x} \left(\lambda \frac{\partial t^*}{\partial x} \right) + \frac{\partial N_i}{\partial y} \left(\lambda \frac{\partial t^*}{\partial y} \right) \right] d\Omega - \int_{\partial\Omega} N_i \underline{q} \cdot \underline{n} \, dS + \int_{\Omega} N_i H \, d\Omega = 0 \quad (2.40)$$

$$-\int_{\Omega} \left[\frac{\partial N_i}{\partial x} \left(\lambda \sum \frac{\partial N_j}{\partial x} t_j \right) + \frac{\partial N_i}{\partial y} \left(\lambda \sum \frac{\partial N_j}{\partial y} t_j \right) \right] d\Omega - \int_{\partial\Omega} N_i \underline{q} \cdot \underline{n} \, dS + \int_{\Omega} N_i H \, d\Omega = 0 \quad (2.41)$$

Using the global reference system, the equations can be written in matrix-vector notation as follows:

$$[K] \underline{t} = \underline{r} - \underline{s} \quad (2.42)$$

where

$$K_{ij} = \int_{\Omega} \left[\frac{\partial N_i}{\partial x} \left(\lambda \frac{\partial N_j}{\partial x} \right) + \frac{\partial N_i}{\partial y} \left(\lambda \frac{\partial N_j}{\partial y} \right) \right] d\Omega = 0 \quad (2.43)$$

is a $n \times n$ global shape function matrix

t_j are the temperature value at the j -th mesh node

$$s_i = s_i^1 + s_i^2 + s_i^3 = \int_{\partial\Omega_1} N_i q_1 dS_1 + \int_{\partial\Omega_2} N_i q_2 dS_2 + \int_{\partial\Omega_3} N_i q_3 dS_3 \quad (2.44)$$

is the global n - component vector representing the boundary conditions (in the boundary $\partial\Omega_1$ is defined a Dirichlet condition, in the part of boundary $\partial\Omega_2$ is defined a Neumann boundary while in the boundary $\partial\Omega_3$ is defined a Robin condition), and

$$r_i = \int_{\Omega} N_i H d\Omega \quad (2.45)$$

is the n -dimensional vector representing the internal heat generation.

Using a local reference notation, the elements of the matrix K can be written as follows:

$$K_{ij} = \sum_{e=1}^m \int_{\Omega^e} \left(\frac{\partial N_i^e}{\partial x} \lambda \frac{\partial N_j^e}{\partial x} + \frac{\partial N_i^e}{\partial y} \lambda \frac{\partial N_j^e}{\partial y} \right) d\Omega^e = \sum_{e=1}^m K_{ij}^e \quad (2.46)$$

(K_{ij}^e is the $r \times r$ local reference matrix)

$$\text{while } t_i = \sum_{e=1}^m t_i^e \quad (2.47)$$

and s is given by

$$\begin{aligned} s_i &= s_i^1 + s_i^2 + s_i^3 = \int_{\partial\Omega_1} N_i q_1 dS_1 + \int_{\partial\Omega_2} N_i q_2 dS_2 + \int_{\partial\Omega_3} N_i q_3 dS_3 = \\ &= \sum_{e=1}^m s_i^{1e} + \sum_{e=1}^m s_i^{2e} + \sum_{e=1}^m s_i^{3e} = \sum_{e=1}^m s_i^e \end{aligned} \quad (2.48)$$

obtaining the same final result. The equations are now evaluated at the element level and the global system is obtained by summing all the elements.

$$\sum_{e=1}^m ([K]^e \underline{t}^e) = \sum_{e=1}^m (\underline{r}^e - \underline{s}^e) \quad (2.49)$$

A typical finite element software computes all the matrices in the local reference and then provides the final global matrix assembly. This procedure allows memory to be saved during the computation. Finite element software in fact calculates the global $n \times n$ matrix by assembling the $r \times r$ matrixes.

In case of linear differential equation, one ends up a linear system and its solution is fast and simple, while if the equations are not linear (like in the case of Navier Stokes equations) the system must be solved using iteration techniques.

2.5.2.1 FEM Time dependent study

The basic principle used for the solution of a partial differential time dependent equation employing the FEM is described here for the equation of transient conduction.

This equation in a bi dimensional domain assumes the form

$$\rho c_p \frac{\partial t}{\partial g} - \left[\frac{\partial}{\partial x} \left(\lambda \frac{\partial t}{\partial x} \right) + \frac{\partial}{\partial y} \left(\lambda \frac{\partial t}{\partial y} \right) \right] - H = 0 \quad (2.50)$$

The parabolic behavior of this equation allows to use the same strategy as in the finite differences case. The time variable is discretized with a time marching method as follows:

$$[C] \frac{t^{n+1} - t^n}{\Delta g} + \gamma [K] t^{n+1} + (1 - \gamma) [K] t^n = \underline{s} \quad (2.51)$$

where γ is the temporal weight parameter identifying a specific case within a class of different methods. In particular if $\gamma=0$ the resulting method is the same as the explicit method described in section 2.4.1.1, while if $\gamma=1$ the method is the same as the finite difference method described in section 2.4.1.2

The previous equation can be rewritten in the following form:

$$\left(\frac{1}{\Delta g} [C] + \gamma [K] \right) t^{n+1} = \left[\frac{1}{\Delta g} [C] - (1 - \gamma) [K] \right] t^n + \underline{s} \quad (2.52)$$

Introducing the auxiliary notations:

$$\frac{1}{\Delta g} [C] + \gamma [K] = [H] \quad (2.53)$$

$$\left[\frac{1}{\Delta g} [C] - (1 - \gamma) [K] \right] t^n + \underline{s} = \underline{f}^n \quad (2.54)$$

the system of linear equations solved by FEM software at each time step is $[H] t^{n+1} = \underline{f}^n$

2.6 Upwinding methods

This technique is adopted in the thermal-fluid models to solve the oscillation problem that appears in the case of strong convective flux. In order to describe the method, the one - dimensional energy equation in its complete form is considered:

$$\rho c_p \left(u \frac{\partial t}{\partial x} \right) = \lambda \left(\frac{\partial^2 t}{\partial x^2} \right) + H \quad u \frac{\partial t}{\partial x} = a \left(\frac{\partial^2 t}{\partial x^2} \right) + \tilde{H} \quad (2.55)$$

By applying the finite element method to an internal node i , the discrete equation is:

$$K_{ij} t_j + f_i = 0 \quad (2.56)$$

where:

$$K_{ij} = \int_L W_i u \frac{dN_j}{dx} dx + \int_L \frac{dW_i}{dx} k \frac{dN_j}{dx} dx \quad (2.57)$$

$$f_i = \int_L W_i \tilde{H} dx \quad (2.58)$$

For constant values of u , a , \tilde{H} , linear shape functions, Galerkin weighting ($W_i = N_i$) and elements of equal size Δx , a typical assembled equation assumes the form

$$(-Pe - 1)t_{i-1} + 2t_i + (Pe - 1)t_{i+1} + \frac{\tilde{H}(\Delta x)^2}{a} = 0 \quad (2.59)$$

where:

$$Pe = \frac{u\Delta x}{2a} \quad (2.60)$$

is the Peclet Number. The above is, incidentally, identical to the typical central finite difference approximation obtained by considering

$$\frac{dt}{dx} \cong \frac{t_{i+1} - t_{i-1}}{2(\Delta x)} \quad (2.61)$$

and

$$\frac{d^2 t}{dx^2} \cong \frac{t_{i+1} - 2t_i + t_{i-1}}{(\Delta x)^2} \quad (2.62)$$

The accuracy of the numerical solution deteriorates as the parameter Pe increases. and when $Pe \rightarrow \infty$ (i.e. when the convective term dominates) the solution is purely oscillatory and does not describe the behavior of the underlying physical problem.

Motivated by the fact that the propagation of information is in the direction of the

velocity u , the upwinding method overcomes this issue of stability by using one-sided finite differences to approximate the first derivative. Thus in place of equation 2.61 the approximation is described as

$$\frac{dt}{dx} \cong \frac{t_i - t_{i-1}}{\Delta x} \quad (2.63)$$

for positive velocity u .

Equation 2.59 can now be written as follows:

$$(-2Pe - 1)t_{i-1} + (2 + 2Pe)t_i - t_{i+1} + \frac{\tilde{H}(\Delta x)^2}{a} = 0 \quad (2.63)$$

With the upwinding difference approximation, realistic (though not always accurate) solutions can be obtained within the whole Peclet number range. In the specific case of convective flux, the employment of an upwinding method is equivalent to increase the diffusion term (or to add a so called “artificial diffusion” term).

The upwinding method can also be introduced in the finite element methods by replacing the weight function $W_i = N_i$ with a modified weight functions W_i^* . The method proposed by Petrov-Galerkin is an example of upwinding technique [4].

3. CAVITY PRODUCTION AND PROCESSING

3 Introduction

The performances of superconducting cavities are strongly affected by the quality of their RF surface [5]. In fact the superconducting currents flow in a surface layer which is only a few nanometers thick. This layer should be as free from defects as possible. Insufficient degreasing, variation of the grain structure and, in general, surface damage caused by the material forming process and later by the machining of the cells themselves can all degrade the cavity performance. These effects manifest themselves in two major limiting phenomena: field emission and multipacting.

Multipacting is a phenomenon of resonant electron multiplication. In high energy particle accelerators, it leads to the build-up of a large number of electrons which eventually form an electron avalanche, leading to power losses and heating of the walls, so that it becomes impossible to increase the cavity fields by raising the incident power [5].

This effect can seriously limit the performance of the cavity. Therefore a lot of precautions are taken to avoid particle contamination and generally to improve the cavity performances. A great number of studies and the experience have demonstrated that the RF performance of a cavity in the superconductive state is increased by the employment of cavities with a particular geometry and by the polishing of the cavity surface. The shape has been largely optimized in the past fifteen years, mostly thanks to the availability of powerful tri-dimensional simulation codes. Right now the Tesla, re-entrant and low loss shapes are much more effective in reducing multipacting with respect to the original pill box. Nevertheless, multipacting can still happen in particular areas of the cavity, as was recently discovered in several high order modes couplers [6]. The introduction of chemical polishing and high pressure rinse additionally reduced the possibility of multipacting and field emission.

Great care is taken during cavity processing and assembly to keep the RF surface as clean as possible; for this reason all the assembly operations are performed in class 10 clean rooms. At the moment many laboratories are pursuing a strong R&D program to increase the average accelerating gradient of the cavities and, to this end, they are experimenting several new techniques for obtaining a smooth and clean RF surface. It has been found that a gradient of 25 MV/m may be consistently achieved if the following typical processing recipe is adopted:

1. External chemical polishing with a removal of a 30 μm surface layer to remove impurities, increases the thermal heat exchange with superfluid helium and limits furnace contamination during heat treatments.
2. Internal chemical polishing with a removal of 150 μm to eliminate the surface damaged layer created during the cavity fabrication process.
3. Annealing heat treatment at 750-800 C to allow for hydrogen degassing.

4. Internal chemical polishing with a removal of 50 μm to eliminate the contaminants surfaced during the heat treatment.
5. Low temperature bake at 120 C to remove Q-drop [7] (physical underling phenomenon still under investigation a brief explanation should be added as a footnote).
6. High pressure rinse at 100 bar of the RF surface to remove any loose particles.
7. Assembly in clean room.

3.1 Advantages and limitations of superconducting cavities

The fundamental advantage of superconducting cavities with respect to the normal conducting ones is the extremely low surface resistance and the high quality factors. Superconducting cavities typically work in the range between 4.5 and 2K. In this range the BCS and residual resistance [8] are the two dominating components and can be as low as 10 nOhms, at least five order of magnitude lower than the copper used for normal conducting cavities. In addition to this, the intrinsic quality factor, Q , for high performing cavities can be as high as 10^{11} . The quality factor is the ratio between the energy stored in the cavity and the one dissipated during one RF period, thus offering a measure of the number of oscillations a resonator will go through before dissipating its stored energy. Furthermore, despite of the low efficiency of the helium refrigeration system there are considerable savings in primary electric power to be had by choosing superconducting RF cavities instead of the equivalent normal conducting ones.

The physical limitation of SC resonators is given by fact that, in order to operate properly, the superconductor must be kept within the vortex free state corresponding roughly to the Meissner state. To be more precise the working area is more extended with respect to the Meissner since the vortexes need some time to generate and penetrate the surface of the material and this time is a few orders of magnitude longer than the RF period. For this reason the RF critical field or superheating critical field is much higher than the regular first critical field under DC conditions. The surface field limitations translate, with the present ILC cavity shape, into an average accelerating gradient limit of $\sim 60 \text{ MV/m}$.

In reality the theoretical limit is very hard to reach since many factors can lower the real operating gradient of the cavity. Even the Q versus accelerating gradient curve, in theory, should be a flat line that stops with a vertical drop corresponding to a quench, in reality the presence of field emission, multipacting and the formation of hotspots affect the slope of the curve in many different ways [9].

3.2 Heat conduction in Niobium

The heat produced by the RF field at the inner cavity surface has to be guided through the cavity wall to the superfluid helium bath. Two factors characterize the heat flow: the thermal conductivity of the bulk niobium and the temperature drop at the niobium-helium interface known as Kapitza resistance. For niobium with a residual resistivity ratio (RRR is defined as the ratio of resistivity at room temperature and at 4.2 K and is a qualitative parameter to identify the purity and the

3. Cavity Production and Processing

thermal properties of the material) [10] of 300, the two contributions to the temperature rise at inner cavity surface are about equal. The thermal conductivity of niobium at cryogenic temperatures scales approximately with the RRR as:

$$\lambda(4.2K) \approx 0.25RRR [W / mK] \quad (3.1)$$

However, λ is strongly temperature dependent and drops by about 1 order of magnitude when lowering the temperature to 2 K [9].

3.3 Cavity Geometry

For practical application the accelerating resonators are made out of multiple cells. This solution allows one to maximize the active length of the linac and at the same time to minimize the number of power couplers, high order mode (HOM) couplers and bolted flanges. However the cell number is limited by several factors such as the difficulty to reach the proper field flatness and the power limitation of the main coupler. Given the performance of the present hardware, ILC cavities have 9 cells as illustrated in *Fig 3.1*.

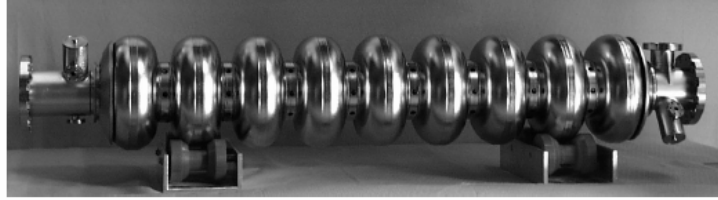


Fig. 3.1 Tesla shape 9-cell cavity.

The cell shape depends on several factors of which the following are the most fundamental:

- A spherical contour near the equator for low sensitivity to multipacting.
- A large iris radius to reduce wake field effects (have these been defined somewhere? Otherwise a footnote or a reference should be inserted).
- The axial dimension is determined by the inversion of the electric field within the time a relativistic particle travels from one cell to the next. The separation between two irises is therefore $c/(2f)$.

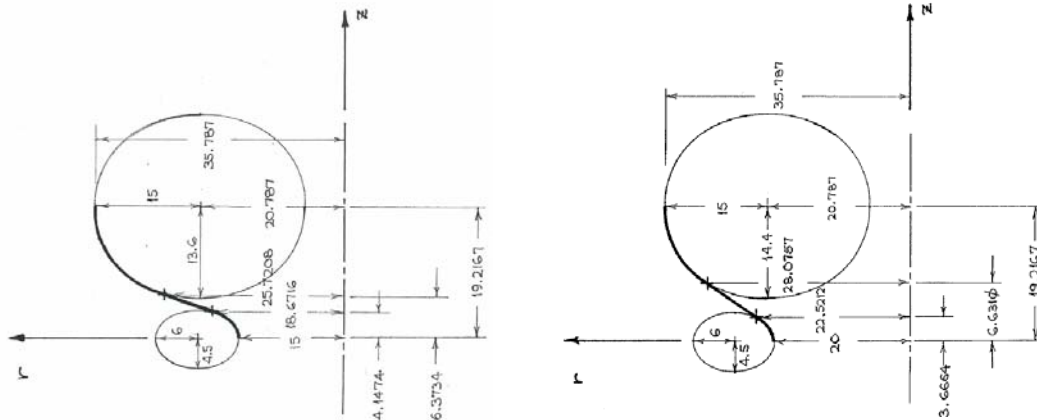


Fig. 3.2 Cavity 3.9 GHz: Mid Semi-Cell.

Fig. 3.3 Cavity 3.9 GHz End Semi-Cell.

The contour of a 3.9 GHz cavity half-cell is shown in *Figure 3.2*. The half-cells at the end of the 9-cell resonator (*Figure 3.3*) is slightly different shape to ensure equal electro-magnetic field amplitudes in all 9 cells [9].

The Cavity geometrical parameters are resumed in the follow *Table 3.1*.

| | | Mid semi cell [mm] | End semi cell [mm] |
|----------------------------------|---------------|-----------------------|-----------------------|
| Half cell length | h_z | 19.2167 | 19.2167 |
| Iris Radius | r_{iris} | 15 | 20 |
| Equator Radius | $r_{equator}$ | 35.787 | 35.787 |
| Iris tangent ellipse midpoint | z_i | 0.0 | 0.0 |
| | r_i | 21.0 | 26.0 |
| Major axis diameter | a | 12 | 12 |
| Minor axis diameter | b | 9 | 9 |
| Equator tangent ellipse midpoint | z_e | 19.2167 | 19.2167 |
| | r_e | 20.787 | 20.787 |
| Major axis diameter a | | 30.0 | 30 |
| Minor axis diameter b | | 27.2 | 28.8 |
| Tangent Point 1 | z_1 | 4.147351 | 3.6664 |
| | r_1 | 18.671631 | 22.5212 |
| Tangent point 2 | z_2 | 6.373441 | 6.6310 |
| | r_2 | 25.720822 | 28.0757 |

Tab 3.1 Cavity Cell profile (Revised).

3.4 Cavity Fabrication

In the early days lead was used to fabricate superconducting RF cavities and later it was substituted by niobium, which presents better superconducting properties. In particular the Meissner phase in niobium extends up to 120 mT allowing considerably high electric fields to be reached on the surface of the cavity. Nowadays there is a strong R&D effort investigating the possibility of using high temperature superconductors such as MgB_2 for cavity fabrication, but niobium still remains the only material currently suitable for near future applications in accelerator technology. There are several techniques utilized for the fabrication of elliptical cavities, which can be classified in two main categories: bulk niobium formation and thin film deposition.

The most common technology involves the formation of cavities from bulk niobium. The material in sheets can be shaped by deep drawing or spinning, while tubes can be hydroformed. Hydroforming and spinning allow formation of a full 9-cell cavity starting from a single precursor. Deep drawing is used to form half-cells that later are electron beam welded to create dumb-bells and finally the full 9-cell cavity. In The deep drawing fabrication process is described in a little more detail below.

3. Cavity Production and Processing

The dies for deep drawing are typically made from a high yield strength aluminum alloy. To achieve the small curvature required at the iris an additional step of coining is added between two separate deep drawing stages.

After the forming process the half-cells are machined at the iris and equator. At the iris the half-cells are cut to the specified length while at the equator an extra length of 1 mm is left to retain the possibility of a precise length trimming of the dumb-bells after frequency measurements.

The accuracy of the shape is checked by sandwiching the half-cells between two metal plates and by measuring their resonant frequency.

The half-cells are then thoroughly cleaned by ultrasonic degreasing, 20um chemical etched at the equator in the weld preparation area and they are then rinsed using ultra pure water. Two half-cells are then joined at the iris with an electron beam welding process to form a dumb-bell. The electron beam welding is usually performed from the inside to ensure a smooth weld seam at the location of the highest electric field in the resonator. Since niobium is a strong getter material for oxygen it is important to carry out the electron beam welding in high vacuum.

Afterwards, frequency measurements are performed on the dumb-bells to determine the correct amount of trimming at the equators. A visual inspection followed by a 30um etch of the equator area allow finding of possible defects [11]. If defects are discovered as a result of foreign material imprints from previous fabrication steps, they are removed by grinding. After the inspection and proper cleaning eight dumb bells and two beam-pipe sections with attached end half-cells are stacked in a precise fixture to carry out the equator welds, which are done from the outside. At this point the full cavity is fabricated and the surface processing starts.

3.5 Cavity Processing

The surface processing of a superconducting cavity is rather complex and involves several steps. Since a golden recipe has not yet been identified and since some of the steps are only necessary for very high gradients, many technologies, alternative to each other, are employed. Essentially the basic recipe includes large material removal, annealing, small material removal and high pressure rinsing. The material removal can be performed utilizing three methods: buffered chemical polishing (BCP), electropolishing (EP) and centrifugal barrel polishing (CBP). Each of these techniques have advantages and disadvantages that will be discussed below.

3.5.1 Chemistry of Niobium

Tantalum with a typical concentration of 500ppm is the most common metallic impurity in high RRR niobium. Among the interstitially dissolved impurities, oxygen is dominant due to the high affinity of Nb to it above 200 C [9]. Distribution of oxygen in the superficial layer of the material seems to be responsible of the Q-drop phenomenon at high gradients.

A natural Nb₂O₅ layer with a thickness of about 5 nm is present on the niobium surface. Below this natural layer other oxides can be found. Nb₂O₅ has a particular structure, able to accommodate many stoichiometry defects [11].

3.5.2 Mechanical Polishing

Centrifugal barrel polishing (CBP), also called tumbling, is a common technique used in industry for surface finishing [12]. A layer of niobium can be removed from the surface of cavities by the friction of thin grains against the walls. CBP was introduced into cavity processing by DESY and KEK. This procedure involves filling up the cavity by grinding stones and water and rotating the cavity at high speed for several hours (*Fig. 3.4*). The standard KEK recipe is divided in 4 steps. During each step the shape and the material of the grinding agent is changed so as to reach a smooth surface. At the end of a successful procedure the weld seam at the equator is hardly visible. Since the grinding process produces a considerable amount of heat, some concern has risen about the possibility of driving large amounts of hydrogen into the material. Although the annealing process should take care of eliminating hydrogen, several studies have been performed with the goal of eliminating water from the process thus reducing the possibility of hydrogen adsorption.

CBP prior to wet chemistry has many advantages. One of them is that it prepares the surface of the cavity for wet chemistry by removing the worst defects such as scratches and by making the surface more uniform. In addition, by substituting the large material removal step, usually performed by BCP or EP, CBP leads to an overall reduction of the environmental impact of the cavity fabrication process reducing the amount of used acid. Finally CBP is well matched with further chemical processes in terms of field flatness preservation. In reality, due to the larger centrifugal force, CBP is more effective at the cavity equator while the chemical processing is more effective at the iris where the fluid velocity is higher. As a result the combination of the two techniques allows for more uniform material removal over the entire cell.

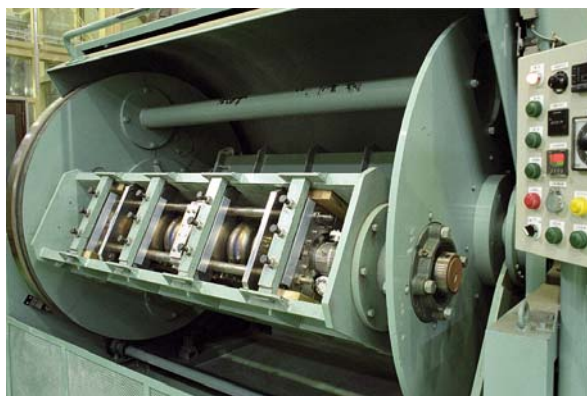


Fig. 3.4 Centrifugal Barrel Polishing.

3.5.3 Chemical Polishing

Nb_2O_5 is a very stable oxide that can be dissolved only by hydrofluoric acid. HF is in fact the essential ingredient used in both the chemical etching techniques used in niobium cavity fabrication and in electropolishing (EP) and buffered chemical

3. Cavity Production and Processing

polishing (BCP) [11].

Polishing the niobium surface with chemicals is the most practical way to achieve reproducible results on the large inner ($\sim 1\text{m}^2$) surface of the 1.3 GHz cavities. The use of HF requires the adoption of very high safety standards. This acid is very harmful, and at the concentrations used for practical applications, the effects to its exposure are delayed in time making the diagnosis hard to identify. For this reason most the facilities used for the chemical etching of niobium present in several laboratories, are remotely monitored and controlled to minimize the possibility of acid exposure.

3.5.3.1 Electropolishing (EP)

At present electropolishing is considered the technology with the most promising capability of producing high performance Niobium SRF cavities. Sharp edges are effectively smoothed and a very glossy surface can be obtained. EP is considered to be the step most responsible for allowing up to 53MV/m in single cell low loss cavities to be reached [13]. During the EP process, the removal of material by electrochemical reaction is induced by applying an electric field between the anode (the cavity) and an aluminum cathode immersed in a mixture of hydrofluoric and sulfuric acids. The most widely used electrolyte is a mixture of concentrated HF and concentrated H_2SO_4 in volume ratio of 1:9.

The chemical processes are summarized in *Figure 3.5* as follows:

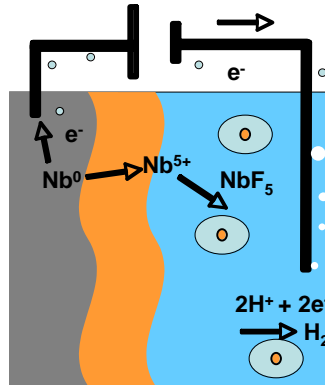
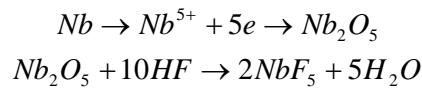


Fig. 3.5 EP process: chemical reactions.



Most systems are horizontal as shown in *Figure 3.6* so that the hydrogen gas produced during the process can be vented from the cavity without the risk of having small bubbles imploding near the niobium walls and creating contamination and formation of imperfections.

The main drawback of this technique is that the process is not fully understood and that the results of its application to the cavities are not easily reproducible or

consistent with expectation. For this reason, at the moment, the SRF community is pursuing a strong research program with the goal of defining the parameter space of EP which will allowing stabilization of the performance for cavities processed with this technique.

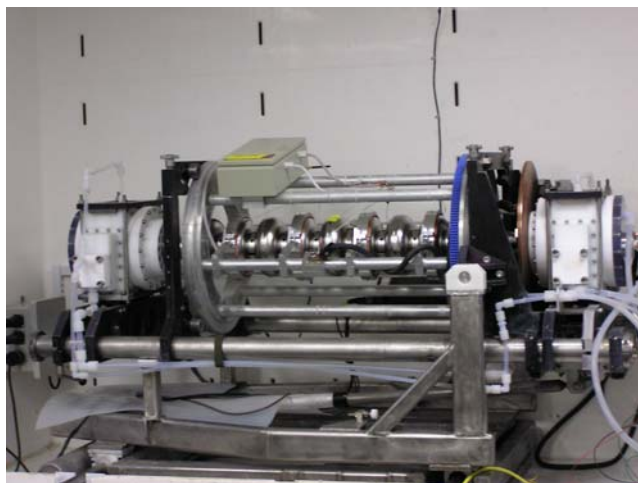


Fig. 3.6 EP facility set-up.

3.5.3.2 Buffered Chemical Polishing (BCP)

BCP has been used in SRF for many years and is considered the most stable and reliable material removal process [14]. Its bigger drawback is that the chemical etching is enhanced at the grain boundaries so that the surface roughness is *increased* by two orders of magnitude. For cavities up to 25-30 MV/m this process is absolutely acceptable but for higher gradients it seems to be the limiting processing step.

This issue could be overcome by switching to large grain or single crystal material. As a matter of fact it was demonstrated at Jefferson Laboratory [15] that a single cell large grain material cavity which had undergone BCP had the same surface roughness and an electropolished one.

This process will be described and discussed in more detail in the following paragraphs.

3.6 Comparison of BCP and EP surfaces

As stated before, EP is now the mainstream process for material removal of ILC cavities. The main reason for choosing this process is the resulting smoothness of the Nb surface that in principle is key factor in achieving higher accelerating gradients. In the *Figure 3.7* BCP and EP treated niobium samples are compared. It is possible see that the BCP does not smooth out the grain of boundaries as well as EP. More precisely, while after EP the surface average roughness is lower than the initial value, after a BCP process the roughness is higher with respect to the initial value due to the preferential etching at the grain boundaries.

The average roughness R_a of chemically etched niobium surfaces is in the order of

3. Cavity Production and Processing

$R_a = 1\mu\text{m}$. The step height on etched surfaces at grain boundaries can even be of the order of a few μm . In the electron beam - welded area at the equator, which is also the region of the highest magnetic surface field, the steps can be as high as $30\mu\text{m}$ and are nearly perpendicular to the magnetic field lines [11].

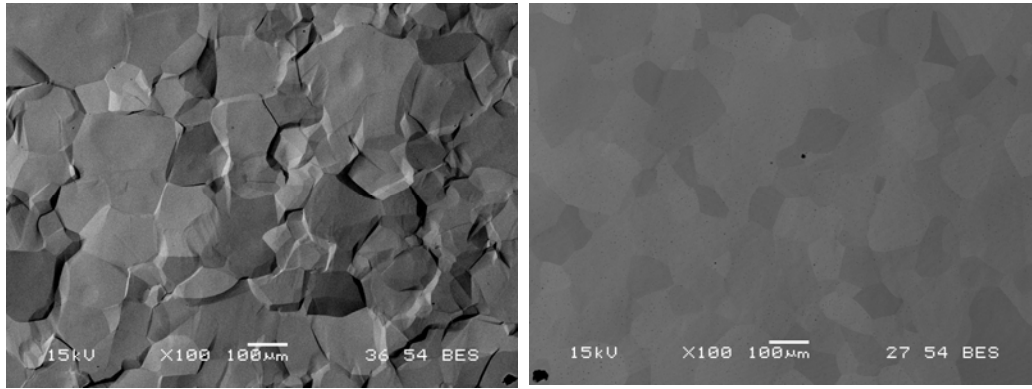


Fig. 3.7 Niobium surfaces after BCP etching (left) and EP etching (right).

It is well known that surface roughness can lead to geometric field enhancements and therefore to a local breakdown of superconductivity at lower field. The roughness of the EP surface is typically one order of magnitude lower than that of an etched sample on length scales larger than $10\mu\text{m}$ as can be seen in the follow figure (Fig. 3.8):

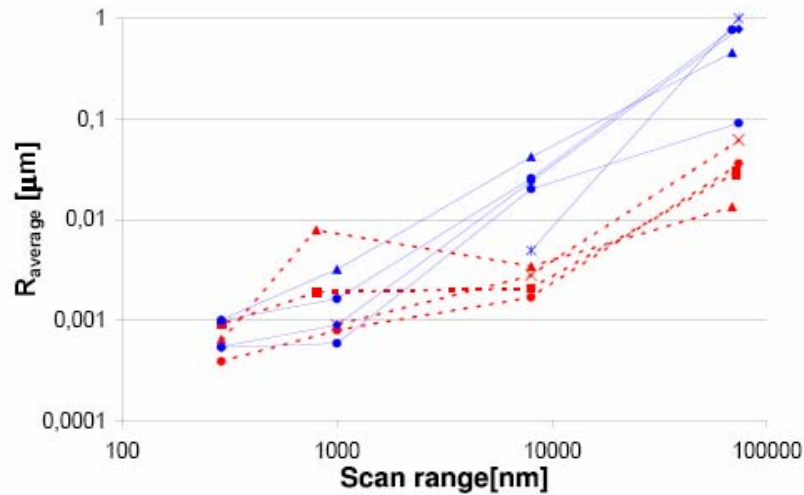


Fig. 3.8 Average roughness as a function of the scan length of the atomic force microscope. EP samples are shown with dotted lines, while BCP samples are shown with full lines. At large scan length EP yields about one order of magnitude lower average roughness than BCP. At lower scan length the difference between EP and BCP becomes smaller. The reason is that at small scan length, one stays on top of a single grain, whereas for large scan length the grain boundaries give the main contribution to the roughness[11].

3.7 Heat treatments

After the large material removal, the cavities are heated to 800 C for 2 hours in a ultrahigh vacuum (UHV) furnace. This step serves two purposes: the removal of dissolved hydrogen from the bulk niobium and the annealing after the deep drawing and welding. In some cases the cavities undergo an additional post purification heat treatment. In this case they are re-heated to 1300 C for four hours. At this temperature all dissolved gases (oxygen, nitrogen and carbon) diffuse out the material. To capture the oxygen coming out of the niobium and to prevent oxidation by the residual gas in the oven (pressure $<10^{-7}$ Pa), a titanium is placed in the furnace with the cavity. The titanium forms a thin layer on the cavity that is removed by a subsequent 80 μ m BCP. A low temperature bake that eliminates the Q-drop phenomenon is also used for high gradient cavities. This heat treatment, performed for 48 hours at 120 C, seems to have an effect on the distribution of oxygen just below the Nb₂O₅ layer [9].

3.8 High Pressure ultra pure water rinsing

After the heat treatments and chemical polishing steps the cavities are mechanically tuned to adjust the resonance frequency to designed value and to obtain equal field amplitudes in all 9 cells. This process is followed by high pressure water rinsing: in order to remove the residual surface contaminations a jet of ultra clean water with a pressure of around 100 bar is swept over the niobium surface. The mechanical force of the water jet washes particles away very efficiently leaving an almost particle free surface.

After this process, the cavity is dried in a class 10 clean room environment and prepared for final assembly. The assembly stage is very critical since it can be source of additional contamination[9].

4. BUFFERED CHEMICAL POLISHING (BCP)

4 Introduction

Buffered chemical polishing is a cheap, simple and effective processing technique for single grain high gradient and polycrystalline lower gradient cavities (25-30 MV/m accelerating gradients).

At present several manufacturers are attempting to produce high purity single crystal ingots at least 10.5" in diameter, which would allow to produce, after slicing, single crystal cells for 1.3GHz cavities. Up to the present time, ingots of only 7" were obtained. The main technical challenge is to slowly melt the material with an electron beam while keeping the liquid bath at uniform temperature in order to obtain a uniform cooling and limit the formation of several crystallographic orientations. The ingot thus produced is then sliced in disks which are used to form half-cells. At the moment several laboratories are optimizing techniques to cut the slices while limiting the contamination of the material. One big advantage of the single crystal material is that by avoiding the hot forging and the rolling RRR value higher than 500 can be achieved. Recently DESY produced a single cell 1.3 GHz cavity using single crystal material. Since the original dimensions of the disks were not large enough, the niobium was rolled in several steps preserving its structure. After formation of the half-cells, they were electron beam welded to form the cavity taking care of aligning the crystal orientation of the cells. This procedure resulted in the production of the first single crystal cavity [16]. This test also demonstrated that a single crystal cavity processed with BCP reached the same surface roughness as electropolished cavities. Were this procedure to be completely qualified this alternative fabrication process could be much cheaper than the standard one and BCP could be used for high gradient cavities.

In the case of polycrystalline niobium BCP does not high gradients to be reached due to the fact that the acid preferentially attacks at the grain boundaries so that the surfaces are not as smooth as they can be achieved with electro-polishing.

Moreover, BCP produces a differential material removal between iris (internal region of the cell) and equator (external region of the cell). Due to their dimensions and shape the 3.9 GHz cavities produced at Fermilab are very sensitive to this phenomenon. In order to resolve the problem, a novel device that can be inflated in the cavity so as to divert the flow in the cell and equalize the etching rate has been evaluated and discussed in the present work.

4.1 Chemistry of the process

BCP uses a mix of three acids: Hydrofluoric HF (49% wt), Nitric HNO₃ (69.5% wt), and Orthophosphoric H₃PO₄ (85% wt). Nitric acid reacts with Nb to form di-Niobium pent-oxide Nb₂O₅. Hydrofluoric acid reacts with this pent-oxide to form hydrosoluble Niobium Fluoride NbF₅. Orthophosphoric acid serves as a buffer helping in keeping constant the reaction rate, which depends on the temperature and

concentration of Nb in the solution (figure 4.1). Although different laboratories use slightly different proportions of the mix, is the volumetric proportion of 1:1:2 (HF : HNO₃ : H₃PO₄) is typical. The removal material rate, and thereby the reaction heat generation, depend on fluid temperature and on the acid velocity. However in order to simplify the modeling; the etching rate was assumed constant for the whole surface of the cavity with a value of 1 μm/min. Under these hypothesis the measured reaction enthalpy H_{rxn} is 700 kJ/mol. The reaction heat generation can be directly obtained from the reaction enthalpy and the etching rate from the next simple relation:

$$1.5373 \times Etch\ Rate \left[\frac{\mu m}{min} \right] \times H_{rxn} \left[\frac{kJ}{mol} \right] = Heat \left[\frac{W}{m^2} \right] \cong 1200 \frac{W}{m^2} \quad (4.1)$$

Based on the existing experience, the rule of thumb suggests keeping the acid temperature below 20°C and concentration of Nb in the BCP bath below 15 g/l. Therefore, a minimum of about one liter of BCP is needed to remove 1 μm of Nb for each 1 m² of treated surface area. As a result, for a typical cavity processing cycle, the required amount of polishing mix can exceed 100 liters. This translates into the need for significant attention to issues of personal and environmental safety and results in the concept of a remotely controlled process.

An immediate (and harmful) byproduct of the process is Nitrogen Dioxide NO₂. Five moles of NO₂ are generated for each mole of reacted Nb. With a 1 μm/min etching rate, about 25 g (or ~12 liters) of NO₂ are released each minute from 1 m² of the cavity surface. Besides NO₂, there is also emission of NO, HNO₃, and HF, which are also considered dangerous pollutants. The fumes of HNO₃ and HF are released by evaporation. The evaporation rate of HF is 7 g/(h·m²) at 15°C; for HNO₃, it is 12 g/(h·m²). If the fumes are not captured, concentrations of these gases in the etching room can easily exceed the acceptable limit of 2 ppm. Obviously, the situation can become even worse if an acid spill occurs and the acid evaporation surface increases. The type and amount of gases released during the process necessitate the use of proper ventilation and exhaust fume scrubbing to guarantee minimal exposure of personnel to harmful gases and to avoid environmental contamination.

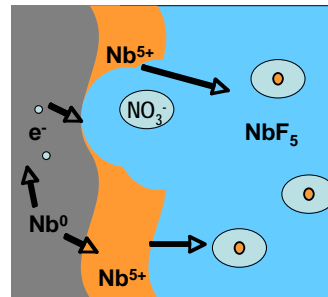
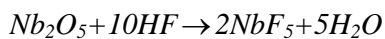
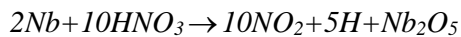


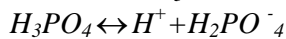
Fig. 4.1 Chemistry of the BCP Etching



Dissolve Nb oxide and expose a new Nb layer



Generated the niobium oxide layer



Buffer

4.2 Description of the Fermilab BCP facility

The main features of the Fermilab BCP facility result from principal process requirements. For example, unless working in a class 10 clean room, the cavity should not be exposed to air for longer than one minute. Longer exposures to air can lead to formation of drying stains, which are hard to remove and usually result in quality degradation. Other requirements include using only ultra pure water for rinsing and preventing unfiltered air from entering the cavity.

The main design concept of the facility is the ability to remotely operate the chemical process from outside the process room where all the acid circuits are confined, thus preventing operators from exposure to acids and fumes [17]. The acid is transported in and out of the room in double contained barrels (HDPE outside, Teflon inside) placed in DOT-approved over-packs (HDPE). Room ventilation is provided with a wet scrubbing system capable of an efficiency of 95% for NO₂ and 99% for the rest of the dangerous gases. The capacity of the scrubber is sufficient for treating one TESLA-type cavity per day and also for manual etching of non-standard parts in acid-filled tanks with an open surface of up to 1 m². By using local ventilation hoods and by monitoring the pollutant concentrations with a gas analyzer, a controlled environment can be created to allow the presence of properly dressed personnel in the room when required.

The layout of the process compartment has been developed based on the request of processing 1.3 GHz 9-cell cavities. The size of the cavities defines the capacity of all tanks, the size of the room, and the footprint of the associated equipment.

The room is 4.5 m in length, 3.5 m in width, and 4.5 m in height. It is lined on the inside with PVC sheets to form a watertight container and is equipped with splash-proof doors. Most of the critical components in the room, like barrels and tanks, are provided with secondary containment vessels; the critical piping circuits are equipped with gutters to contain spills. In the case of a major spill, thanks to a slightly tilted floor, the acid is collected in a trench located along one of the sides of the processing room; the capacity of the trench exceeds the capacity of the acid barrels (250 liters).

The topology of the hydraulic system was developed to minimize the length of piping, to simplify the handling of the barrels with clean and used acid mix, and to provide enough space for personnel to safely install and remove cavities from the process tank and to perform maintenance activities like repairs and cleaning. The parts of the system where the acid cannot be removed (e.g. filter and heat exchanger) are separated from other components by ball valves.

There are three major steps of the BCP process: acid cooling, etching, and rinsing. The system preparation and testing as well as post-process clean-up are equally important for the reliable operation of the facility and for stable and reproducible results.

The BCP process is exothermic: for each mole of etched out Nb, 312 kJ of heat are released into the solution. The chemical reaction rate increases with temperature and there can be a process run-out if the temperature exceeds 20°C. Commonly, during the process, the temperature is kept around 15°C and the acids in the barrel brought into the process room are thoroughly mixed to avoid stratification. The cooling takes place in an immersion style PVDF-made heat exchanger. With the cooling power of 3 kW at 5°C provided by a standard chiller filled with Propylene Glycol, the cooling

time for 250 liters of acid mix is about 2 hours.

Gravity feed tanks are used to meet the important criterion of filling the process tank with acid or water in less than one minute. Since the amount of acid used in the process can be up to 250 liters, using a pump to fill the process tank is not a reasonable alternative. The same idea serves for fast removal of acid or rinsing water out of the process tank. In this case, additional tanks are used to contain acid or rinsing water while it is pumped out of the tanks into a used acid storage barrel or neutralization system.

During the process, when the acid reacts with Nb, the heat generated reaches about 500 W for a ILC-type cavity (treated surface of about 1 m²). An additional 500 W are added by the piping used for the acid circulation due to heat exchange with room air. To keep the temperature under control during the etching, the acid is circulated through the cooling system previously used for the initial acid cooling.

Usually the inner and outer surfaces of a cavity require different depths of etching. To make it possible, PVDF-made jackets are used to protect inner or outer surfaces when they do not need etching. These jackets are filled with ultra pure water that circulates through the same cooling system.

After etching is completed, the acid in the process tank must be promptly replaced with rinsing water. The rinsing is repeated until it is safe for personnel to handle the cavity. Typically several rinsing cycles are required before the pH > 4 is reached, which is considered safe [18].

All the water used for rinsing is treated by a standard automated neutralization system. It detects the acidity of the water and adds the needed amount of a caustic solution for neutralization.

Gases and fumes generated during the process are collected by local hoods and removed by a ventilation system for neutralization by a wet scrubber. The ventilation system has been configured to prevent release of the gases and fumes in the room during normal operation, to provide optional ventilation capacity for a hood used for manual etching inside the room, and to ensure a quick air exchange inside the room in a case of a major spill. The capacity of the ventilation system and the scrubber is about 85 m³/min. The pattern and configuration of the local ventilation points where the contaminated air is extracted can be changed remotely at different stages of the process by using dumpers.

The major air contaminant concentrations are monitored during and after the process to provide the personnel with information on air quality. For this purpose a gas analyzer equipped with two gauges sensitive to HF and NO₂ is used.

Before the make-up air enters the room, it is filtered by a pack of EPA filters installed in the air intake. As an additional protection measure and to ensure the cleanliness of the air that enters the cavity under process, the gravity feed tanks and the process tank are also equipped with filters.

Due to the aggressive nature of acids and fumes inside the process room, measures must be undertaken to ensure reliable functioning of the involved equipment. The use of electrical power circuits inside the room was avoided and all the electrical and pneumatic circuits were protected from exposure to the room environment. All the pumps and the valves in the room are pneumatically driven and are controlled by solenoidal valves mounted outside the room. The Polyethylene compressed air lines are traced to the points of use inside PVC piping with junction boxes at the ends.

The system is equipped with many gauges: sensors for temperature, level, flow rate,

conductivity, acidity, and pressure help monitor the process at different stages. The readings of the gauges are used to provide the needed feedback to the control system and to set control marks for the interlock system that was designed to protect personnel and the processed cavity. The feedback signal cables pass through PVC piping hermetically connected to junction boxes. Between the junction boxes and the points of use (the sensors or read switches) the cables are enclosed in PE piping so that the wiring is not exposed to the aggressive gases.

A semi-automatic operating mode is used to control the process, which is broken into several steps. The system performs each step automatically, but the decision to switch to the next step is made by an operator. The fully automated steps of the process are: acid cooling, gravity tank filling, etching, rough rinse, and fine rinse.

The process control is based on a Programmable Logic Controller (PLC) and is monitored by a computer-based Human-Machine Interface (HMI) [19]. In this case, any failure of a computer system does not affect the process. Built-in back-up power allows safe completion of the process at any stage in case of a major power failure. Once programmed, the PLC can control the process, watch its status through a system of sensors, report the status to the operator, and perform other useful functions, e.g. statistical analysis.

At any time, the facility operator can switch from automatic to manual mode. During manual mode, the operator can directly control all the components with the use of the HMI by clicking on the icons representing the components on a computer screen. An interlock system prevents accidental or unauthorized access to the manual mode.

Since the Fermilab BCP system is still in the process of passing the laboratory safety review, most of the cavities are processed in the ANL facility.



Fig.4.2 Fermilab BCP Facility (Facility 1)

Since both the facilities are of interest, simulations were performed for each of them. The two facilities are very different in terms of layout and of automatization of the process but only few details needs to be taken into account during the modeling.

In the Fermilab facility the cooling jacket is completely immersed in the acid tank (in the follow FACILITY 1) as show in *Figure 4.2* while in the Argonne facility the cooling jacket is a simple plastic container directly in contact with the environmental air (FACILITY 2) like shown in the follow figure (*Fig. 4.3*):



Fig. 4. 3 Argonne BCP Facility (Facility 2)

Next table (*Tab. 4.1*) resumes the main differences between the two facilities relevant for the computational study of the BCP process:

| | | Facility 1 | Facility 2 |
|----------------------------------|----------------------------|------------|------------|
| Acid flow rate | GPM (Gallon Per Minute) | 1.5 | 1.5 |
| Water flow rate | GPM (Gallon Per Minute) | 5 | 10 |
| Acid inlet temperature | K | 288 | 288 |
| Water inlet temperature | K | 288 | 279 |
| Average reaction heat generation | W/m ² | 1200 | 1200 |

Tab 4.1 Facilities parameters relevant for the simulation.

4.3 Differential Etching between iris and equator

Either using EP or BCP the overall removal of material in the cells is not uniform. The local material thickness is measured with an ultrasonic gauge in several spots of the cell both before and after the material removal process. As a result one discovers that the removal rate at the equator is much higher with respect to the one at the iris by a factor varying between 1.3 and 2.

This phenomenon is related to the high viscosity of the acid mix and to the geometry of the cavity. The combination of these two factors favors the stagnation of the acid

within the cells reducing the etching rate. At the contrary the flow rate at the iris is very high increasing the etching rate.

In the case of low frequency cavities it has already been proposed to introduce a system of rigid diverters to force the flow in the cells. In the case of 3.9 GHz cavities, due to their small dimensions, this solution is not feasible due to the high risk of scratching the surface at the end of the process.

As an alternative it was proposed to insert a system of nine PET balloons inside the nine cells cavity. PET samples were tested in acid environment comparable to the BCP process showing good acid resistance after four hours exposure, which is more than twice the duration of a typical cavity etching.

Due to its dimensions the balloon is molded in three separate segments, which are later glued together using the proper bounding technique. For this purpose cyanate and UV cured glues were tested. Several samples of glued PET tubes were immersed for 4 hours in acid environment similar to the standard BCP process. As a result the UV cured glue was chosen being the more reliable.

To complete the insertion device, after assembly the balloon would be mechanically fixed to a PVDF tube that serves also as centering device and inflating system [20].

The balloon geometry is shown in the follow figures (*Fig. 4.4 and Fig. 4.5*).

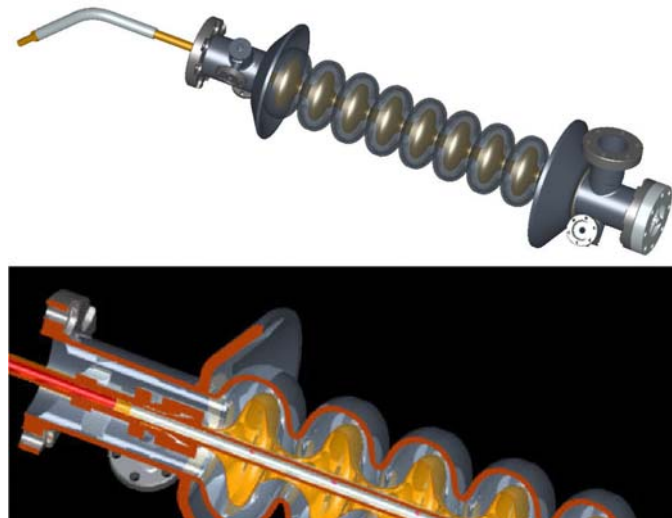


Fig. 4. 4 Flow diverter in the cavity.

4.4 Experimental Verification

A flow visualization experiment was performed in order to verify the numerical simulation and later the effectiveness of the flow diverter. A transparent polyurethane 9-cell cavity was produced and a basic device to introduce small amounts of colored dye in the main stream of water was designed.

The tests were performed using water and, in order to maintain the same Reynolds number, the velocity was proportionally reduced to mimic the acid flow of the BCP process.

The test demonstrated that even if the flow at the center of the cavity is fully

developed, the acid remains trapped in the cell volume leading to differential etching between iris and equator.

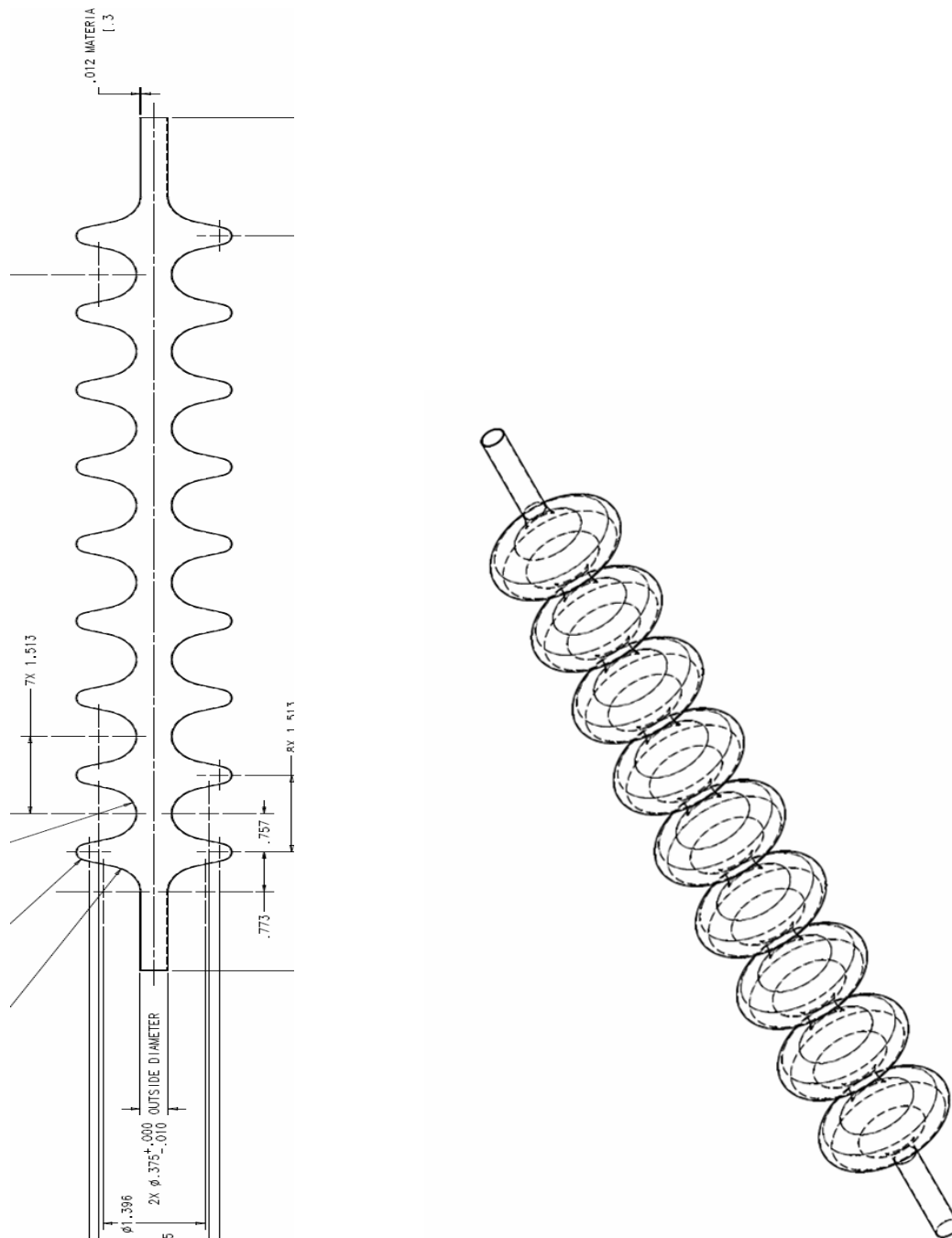


Fig. 4.5 Balloons system geometry

5. SIMULATIONS

5 Introduction

While waiting for the single crystal or large grain technologies to be mature enough for cavity production, it is worth to investigate possible optimizations of the BCP process which can be a valid alternative to electropolishing if the poly-crystal material is abandoned.

The present simulation work was aimed at investigating of the basic mechanisms of BCP and to the physical phenomena governing the process. The modeling ultimately led to an understanding of the origin of the differential etching between iris and equator and eventually helped in finding the proper solution.

The simulations were performed using a commercial finite element software, COMSOL, which is appropriate for the investigation of “multi-physics” problems. The main feature of this software is that it gives the operator full control over the system of partial differential equations used to model the physical system and allows them to be solved simultaneously while taking into account the cross couplings.

Several simulations have been completed using different set of input parameters and solver options in order to verify the consistency of the results. When attacking multi-physics problems the experience of the operator becomes a fundamental factor in reaching convergence to the solution. In our case the coupling between energy conservation and momentum conservation was particularly difficult to handle and require the use of several tricks to reach a converging solution. In this chapter the main techniques adopted during the simulations will be discussed and described.

5.2 Geometry simplifications

As mentioned in chapter 4, two different configurations have been considered for the modeling of the BCP process. The geometry is the same in both cases but the boundary conditions are different. In order to simulate the process one needs to consider the cavity in its cooling jacket as shown in *Figure 5.1*.

The cooling jacket has the follow dimensions:

-radius: 0.1175 m

-height: 0.45 m

The geometrical model has been built in the Comsol 2D draft environment.

Obtaining the acid flow pattern and an average temperature map inside the cavity was the main goal of the thermal-fluid simulations as well as the temperature map of the cooling water. For this reason the choice of an axial symmetrical model fulfills the requirements and allows for fast solutions.

Nevertheless the axial symmetrical model induces a strong approximation on the water flow profile throughout the cooling jacket and on its distribution of temperature. In fact, in the real facility, the water enters in the jacket from the inlet tube and leaves through the outlet tube, while in the axial symmetric representation the water flows in and out of the jacket through an annular area. This approximation

strongly affects the temperature field in the jacket. In order to avoid this issue, one should use a three-dimensional approach, but this would imply longer calculation times with no basic improvement over the knowledge of the process.

5.3 Geometry Generation and Sub-domain definition

In *Fig 3.2 - 3.3* is shown the profile of a 3.9 GHz cell. The axial symmetrical geometrical model shown in *Figure 5.1* has been drawn using the interactive interface of the Comsol 2D draft environment.

The simulation area is divided in three different sub-domains allowing to correctly describe the properties of the three regions characterizing this process:

- CO1 the acid sub-domain
- CO2 the cavity
- CO3 the water sub-domain

In order to parameterize the dimensions of the inlet and outlet water pipes, four points had to be defined. P3 and P4 identify the inlet annular area ($r_{p3} = 0.1$ m and $r_{p4} = 0.075$), while P1 and P2 identify the outlet.

5.4 Mesh type and Processing

A direct time-dependent solver was used for transient simulations while an Eulerian direct solver (UMPFACK) was used for non-linear stationary simulations. In most of the cases the time dependent solution was adopted as a first step to understand the convergence behavior of the problem.

In order to converge to solution in the case of strong convective problems, as explained in the chapter 2, the Peclet numbers $Pe = \frac{u\Delta x}{2a}$ must be maintained as low

as possible. Since the physical parameters u and a are fixed, the only alternative to reduce the value of the Peclet number is the reduction of Δx by a mesh refinement.

An handy feature of Comsol is the “Peclet-cell number visualization” which allows to reduce the mesh only in the domain regions where the Peclet number is high.

As an alternative method one can set opportunely the residual error parameter.

Comsol solves the non linear algebraic systems -introduced by the non linearity of a fluid dynamic problem- using an iterative method.

DEVO CHIEDERE UNA COSA A FASINO QUI:

If the residue error is high the solution can be very accurate but the calculation time would be very long. Hence it is fundamental to define a good compromise between accuracy of solution and calculation time.

Triangular elements have been used in all cases. *Figure 5.2* shows a typical mesh. It can be noticed that along geometrical discontinuities and in areas where high gradients are expected the dimensions of the elements had to be strongly reduced. A good example of mesh optimization is the refinement of the element dimensions at the water inlet in the jacket; this solution takes care of the high temperature gradients

description.

In case of excessive use of memory, it is possible to use quadrangular elements and mapped meshes, which allow to describe very efficiently unidirectional flows. However in our case the triangular mesh and direct solver combination was a good compromise in terms of solving speed and precision of the solution.

Quadratic shape functions have been used to describe the fluid dynamic and chemical environments, while cubic shape functions have been employed in the thermal case.

A parametric direct solver was used in few cases where convergence was hard to achieve.

5.5 Fluid dynamics (Fluid Dynamics Module)

The fluid-dynamic stationary study was the more complex part of the modeling due to the high non-linearity that characterizes the differential equations used to describe this phenomenon. In order to complete this part of the work, a large number of simulations had to be carried out before a converging result could be obtained.

In addition to the intrinsic non-linearity of the Navier-Stokes equations, the complex geometry of the problem posed a number of modeling concerns.

Three main strategies have been adopted to reach convergence in stationary studies:

- Use the result of time dependent solutions for long times as initial value for the stationary model in order to allow starting the simulation from a rather stable point.
- Parametric upwinding study (see chapter 2).
- $k-\epsilon$ Turbulence method.

Although the first technique turned out to be the most reliable one, it is surely the more time consuming. On the other hand, the parametric unwinding technique is the most elegant solution for the stabilization of the solution. As explained in the numerical methods chapter, where numerical methods are discussed, an artificial diffusion coefficient appears in the equations when the upwinding technique is used. The artificial diffusion is added to the model to allow it to reach a first approximate solution which is used this as an initial value for more accurate ones. The amount of artificial diffusion is step by step decreased in the sequence of solutions until it is completely eliminated. This process is automatically performed by Comsol through the parametric study feature.

After several attempts it was confirmed that the $k-\epsilon$ turbulence method cannot be used to reliably improve the stability of this particular type of simulation.

Since the $k-\epsilon$ turbulence method is generally adopted to gain stability in problems where the formation of vortices is an issue, the generation of vortices inside the cells would suggest that the use of this method might be helpful.

However, it is necessary to consider that in the case of low Reynolds number (as in our model) the $k-\epsilon$ method reaches a wrong solution. In fact by looking at the simulation results when this technique is adopted, despite the complex geometry the flow results are completely laminar (*Figure 5.3*), which is not consistent with the experimental evidence.

Mesh refinement was also used as an additional stabilization technique. This method allows to create a finer and personalized mesh in the most critical areas of the model

thus allowing reaching more precise results.

Geometrical and physical discontinuities produce numerical oscillations during the simulation. This aspect has been briefly described in chapter 4 where the Peclet number was introduced as a representative index of the solution stability. The lower the Peclet number, the higher is the possibility to reach solution convergence.

In Comsol it is possible to visualize the local Peclet number as part of the post-processing procedure and refine the mesh in the areas where this number is higher. *Table 5.1* summarized the sub-domain characterization for the fluid dynamic system.

| Property | Unit | CO1 Acid | CO2 Nb | CO3 Water |
|-----------------|-------------------|----------|--------|-----------|
| Density ρ | Kg/m ³ | 1530 | N/A | 1000 |
| Viscosity μ | Pa*s | 0.0221 | N/A | 0.001 |

Table 5.1 Material properties for fluid dynamic simulation.

Due to the vertical position of the cavity, the gravitational force is taken into account. For this reason, in both the acid and the water sub-domains appears the additional term:

$$F_z = -g \cdot \rho \quad (5.1)$$

The fluid-dynamic study was common for both facilities since the acid flow rate is similar. This simulation is a first step toward the full blown model and allows to take into account the behavior of the acid flow inside the cells without having to worry about the stability of the solution of the water pattern in the cooling jacket. One could consider not simulating the water domain at all due to the fact that no thermal effect is taken into account and the water flow has no effect on the acid pattern in the cavity.

The Facility 1 configuration, being the high velocity case, was considered for the fluid-dynamic study. The boundary conditions are shown in *Figure 5.4* and are described below.

5.5.1 Fluid-dynamic boundary conditions

The acid velocity is imposed at the inlet section (section 2) with the following relationship representing the parabolic velocity profile of a fluid that flows inside a pipe:

$$V_{acid} = \frac{3}{2} V_{mac} (1 - s^2) \quad (5.2)$$

where V_{mac} is the average velocity calculated taking into account the fixed flow rate of $Q=1.5$ GPM ($0.000094 \text{ m}^3/\text{s}$) over the fixed cavity inlet area ($A_c = \pi r_{cav}^2$)

$$V_{mac} = \frac{Q}{A_c} = \frac{Q}{\pi r_{cav}^2} = 0.0748 \text{ m/s} \quad (5.3)$$

Where $r_{cav} = 0.02\text{m}$

The variable “s” is automatically used by Comsol as a parameter to describe functions, and present a fixed range between zero and one.

The velocity expressed by 5.2 is an approximation of the real value. In the real case both the acid and the water flows are guaranteed by double acting diaphragm pumps, which generate an half sinusoidal oscillations. Nevertheless assuming an average value for the fluid velocity allows to obtain stationary and transient solution with less stability issues.

The water velocity is imposed at the inlet section (section 3).

In order to achieve the energy balance between the cooling effect of water and the heat of the reaction, the water flow rate was assumed to be $Q_{w1} = 5 \text{ GPM}$ ($0.000315 \text{ m}^3/\text{s}$) for facility 1 and $Q_{w2} = 10 \text{ GPM}$ ($0.000630 \text{ m}^3/\text{s}$) for facility2. The total flow is distributes in the same annular area with a parabolic distribution as described in equations 5.4 and 5.5.

$$V_{w1} = 6V_{mw1} s(1-s) \quad (5.4)$$

$$V_{w2} = 6V_{mw2} s(1-s) \quad (5.5)$$

Where V_{w1} and V_{w2} are the average water velocity in the cooling jacket inlet annular area ($A_j = \pi r_{p3}^2 - \pi r_{p4}^2$) concerning the facility1 and facility2 respectively:

$$V_{mw1} = \frac{Q_{w1}}{A_j} = 0.0229 \text{ m/s} \quad (5.6)$$

$$V_{mw2} = \frac{Q_{w2}}{A_j} = 0.0458 \text{ m/s} \quad (5.7)$$

Although the axial symmetrical model provides an approximate representation of the water velocity field inside the cooling jacket, this configuration presents many advantages. In particular, the water Reynolds' number is lower respect to the real case (where the same flow rate enter through a small section) with a resulting higher model stability.

| | Facility 1 | Facility 2 |
|----------|------------|------------|
| Re acid | 207 | 207 |
| Re water | 1145 | 2290 |

Table 5.2 Low Re numbers are involved in the two facilities ($Re = \frac{\rho v D}{\mu}$, where is the fluid

density, the fluid viscosity, v the fluid average velocity, and D the diameter of the inlet section. In case of annular area the hydraulic diameter is considered

$$D = 4 \frac{\text{wet area}}{\text{wet perimeter}})$$

The laminar flow condition is $Re < 2100$.

Although in the facility 2 the water Reynolds number is higher than 2100, no stability problem was encountered during the simulations. A more precise solution could be obtained by considering separately the physics of the acid and the water domains. In this case the acid domain should be solved using the classical Navier-Stokes module and the water domain using the k- ϵ module.

To complete the boundary conditions one needs to define:

- No slip condition on all walls (sections 6,7,8).
- Axial symmetry condition along the center line of the cavity (section 1).
- Imposed flow at both acid and water outlets (sections 4 and 5).

The numerical simulations results consistently confirmed the flow visualization experiments [20] demonstrating that even if the flow at the center of the cavity is fully developed, the acid remains stagnant within the cell volume (*Fig 5.5* and *Fig 5.6*).

5.6 Thermal-Fluid study (fluid dynamics Module plus convection and conduction Module)

Adding the thermal component to the fluid dynamic model is straight forward and most of the stabilization techniques described so far can be extended to this simulation as well. In this case the two facilities had to be considered separately and two thermal-fluid the evolution of the process for the full length of the BCP process and a stationary study to evaluate the existence of a steady condition.

The comparison between the solution of the stationary problem and the result of the transient calculation demonstrated that the process stabilizes after 300 seconds as shown in *Figure 5.7* and *Figure 5.8*.

The fluid dynamic parameters did not change with respect to the previous models, but the thermal proprieties and the coupling relationships between the two systems had to be added. The Boussinesque law, shown in equation 5.8, was used to link the thermal and the velocity fields.

$$F_z = g \cdot \alpha \cdot \rho \cdot (T - T_{init}) \quad (5.8)$$

where: g is the gravity acceleration

α is the linear expansion coefficient

ρ is density

T_{init} is the system temperature at the initial time $t=0$

This term is added to the total vertical force component resulting in the following equation 5.7.

$$F_z = -g \cdot \rho + g \cdot \alpha \cdot \rho \cdot (T - T_{init}) \quad (5.9)$$

This formulation is a good approximation when close to room temperature as for our case. On table 5.3 are listed the main thermal properties used in this model.

| Property | Unit | CO1 Acid | CO2 Nb | CO3 Water |
|----------|------|----------|--------|-----------|
|----------|------|----------|--------|-----------|

| | | | | |
|----------------------|-------------------|------|------|------|
| Density | Kg/m ³ | 1530 | 8500 | 1000 |
| Heat capacity | J/(kg K) | 2000 | 265 | 4186 |
| Thermal conductivity | W/(m K) | 0.5 | 53 | 0.6 |

Table 5.3 Properties for the thermal model.

The boundary conditions had to be separately defined for the two facilities.

5.6.1 Facility 1 Thermal boundary conditions (Figure 5.4)

- Axial symmetry along the center line of cavity $r=0$ (boundary 1)
- Heat generation due to the chemical reaction along the internal cavity walls in contact with the acid $Q=1200 \text{ W/m}^2$ (boundary 6)
- Convective flux in the acid and water outlets (boundaries 4 and 5)
- Continuity along the cavity walls in contact with the water (boundary 7)
- Imposed Temperature along the cooling jacket walls 288 K (in this facility the cooling jacket is completely inserted into the acid tank, and the acid is maintained at the fix temperature of 288 K. To assume that the cooling jacket wall temperatures and the acid temperature are the same is a realistic hypothesis) (boundaries 8)
- Imposed acid inlet temperature 288 K (boundary 2)
- Imposed water inlet temperature 288 K (boundary 3)

5.6.2 Facility 2 Thermal boundary conditions

- Axial symmetry along the center line of cavity $r=0$ (boundary 1)
- Heat generation due to chemical reaction $Q=1200 \text{ W/m}^2$ (boundary 6)
- Convective flux in the acid and water outlets (boundaries 4 and 5)
- Continuity along the cavity walls in contact with the water (boundary 7)
- Thermal Insulation (in this facility the cooling jacket is a plastic tank in direct contact with the environmental air. Since the jacket plastic walls are thick, the adiabatic hypothesis are completely justified). (boundaries 8)
- Imposed acid inlet temperature 288 K (boundary 2)
- Imposed water inlet temperature 279 K (boundary 3)

5.6.3 Results and discussion

The stationary study of Facility 2 revealed some problems related to the different initial temperatures of acid and cooling water. Under such conditions the simulations do not converge to solution. In order to avoid this issue one can use a technique similar to the one adopted in the fluid dynamic simulation in order to start the stationary simulation from a more stable point. In this case, through a step by step process, the temperature in the three sub-domains were adjusted starting from an equal initial temperature value.

The initial temperature value T_{init} of acid and water was modified toward the correct

values T_{acid} and T_{water} respectively, using opportune Matlab functions, as shown below:

$$T_{init} = 283 \quad (5.10)$$

$$T_{acid} = \min(283 + t, 288) \quad (5.11)$$

$$T_{water} = \max(283 - t, 279) \quad (5.12)$$

Where t is the time variable.

In this case the transient simulation was stabilized after circa 300 sec. Taking the 300th sec as initial value for the stationary simulation, this analysis reached a converging solution as well.

This technique allowed avoiding infinite gradient conditions that would occur for fixed initial values.

The thermal-fluid studies showed that in absence of a strong water-cooling and due to the acid inlet at the bottom cell of the cavity, the cell average temperature raises though the cavity (facility 1) as shown in *Figure. 5.7*.

Furthermore the simulations demonstrated that increasing the cooling capacity by lowering the water input temperature helps optimizing the cell to cell temperature distribution (facility 2) as shown in *Figure. 5.8*.

5.7 Acid and water counter flow

The thermal-fluid studies were completed for both the facilities in the case of water in counter flow with respect to the acid as well (*Fig 5.9* and *Fig. 5.10*).

The goal of this simulation was to understand whether a uniform thermal field could be reached in this configuration. The simulations showed no appreciable differences in the trend of the temperature inside the cavity. As a result it was demonstrated that from the facility setup point of view, there is no difference whether the acid and the water are in parallel or in counter flow configuration.

Reaching a stable solution for this simulation was very complicated due to the presence of counter flow fluids.

This issue was solved by setting the appropriate initial values in both the acid and the water sub-domains. In fact by defining two opposite low initial values for acid and water the system reached a converging solution.

5.8 Chemical Simulation (fluid dynamics Module plus convection and conduction Module plus convection and diffusion Module)

In order to fully simulate the BCP process in all its aspects, one should also take into consideration the chemical reactions and the diffusion of the species in solution. In all previous models the chemical reaction had to be substituted by its heat generation, which was considered constant through the process and uniform on the whole surface. In reality the speed of the reaction depend on both the temperature and the unbalanced concentration of species in solution. As a matter of fact the stagnation of

acid in the cells, which is mostly due to its viscosity and to the geometry of the cavity, lead to the generation of high niobium concentration areas in which the chemical reaction is much slower with respect to fresh acid conditions.

In order to take into account this effect, a third physics was added to the simulation by introducing the equation system regulating the mass transport due to diffusion and convection. Since for transport phenomena the velocity field is the most critical aspect and being the velocity maps very similar for both facilities, this study was performed only for facility 1.

In order to reach the stationary solution, the usual technique of performing a time dependent analysis up to 300 seconds and use the solution as initial value for the steady state analysis was adopted successfully.

As shown in *Figure 5.11* and *Figure 5.12*, this simulation confirmed the high concentration of reaction products within the cells and explained in more detail the reason for slower etching rate at the equator of the cells. *Table 5.4* summarizes the material properties used for this model.

| Property | Unit | CO1 Acid | CO2 Nb | CO3 Water |
|------------------|-------------------|--------------------------------------|--------|-----------|
| Diffusion coeff. | m ² /s | 10 ⁻⁷ or 10 ⁻⁸ | N/A | N/A |

Table 5.4

The exact value of the diffusion coefficient D is unknown since the chemical behavior of the BCP is still being studied and the Einstein Stokes relation could be used for the diffusion coefficient determination.

$$D = \frac{kT}{6\pi\mu R} \quad (5.13)$$

Where: T is the temperature, k is the Boltzmann constant, μ is the acid viscosity, R is the solute (Niobium in our case) radius. Unfortunately also this relationship is too approximate and moreover the R parameter is not known.

In order to solve this issue a set of three coefficients ranging between 10^{-7} and 10^{-9} was used obtaining substantially the same results as shown in *Figure 5.11* (case with $D=10^{-7}$) and in *Figure 5.12* (case with $D=10^{-8}$) [21]. The justification of such result is that the macroscopic effect of the velocity field is dominant for this process and for any given diffusion coefficient, within the given range, the concentration of acid in the cells remained roughly the same and close to saturation. The resulting effect was an overall slowing down of the etching process in proximity of the equator.

The boundary conditions used for the mass transport model are the following:

- Axial symmetry along the center line of cavity $r=0$ (boundary 1).
- Species (Niobium) Concentration $c=1$ along the cavity walls (boundary 6).
- Species Concentration $c=0$ at the acid enter section. (boundary 2).
- Convective Flux in the acid exit section (boundary 4).

5.9 Flow diverter

The three levels of simulations described above: fluid dynamic, thermal-fluid and thermal-fluid with diffusion were repeated in the case of the flow diverter inserted in the cavity. The same strategies were adopted to reach a converging solution as it was

for the case without the flow diverter. The only difference regards boundary condition 1 (*Fig. 5.13*), which in these simulations is modified as follows in the mass transport model:

- No slip in the fluid dynamic module
- Insulation symmetry in the thermal and chemical modules.

In all cases the deformations of the balloons, due to the acid flow, have been neglected. Results for facility 1 are shown in *Figures 5.14* to *Figure 5.17*.

The analysis of the temperature, the velocity and the concentration maps demonstrated that the use of a flow diverter allows to obtain more uniform distributions of the three parameters. The acid stagnation in the cells is avoided by using the balloon system allowing to reduce significantly the differential etching between iris and equators [20].

As an additional step the model was used to optimize the acid velocity in the cavity. In fact by keeping the same flow rate as for the case without the diverter, several vortices could be generated with consequent perturbation of the local flow. This issue was solved by simply reducing the overall acid flow rate until a full laminar flow was observed in the simulations.

5.10 Simulation of ILC 1.3 Ghz cavities

At the moment, at Fermilab, an engineering team is working on a modified design of the 3.9 GHz BCP facility in order to allow processing ILC 1.3GHz cavities. In general these larger cavities have the same volume to surface ratio as the 3.9 GHz. For this reason the simulations performed for the smaller cavities can be proportionally transferred to the larger ones.

However the new design of the facility was developed around the core idea of eliminating the acid gravity feed system and substitute it with a close loop circulation. In addition, and this is what simulations could help understand better, it was decided to investigate the possibility to avoid cooling the acid and simply rely on the water cooling. The main reason behind this choice is that cooling the acid during the process means having to deal with complex plastic heat exchangers with rather large surface. Plastic heat exchangers can tolerate acid for long periods of times but it is not simple to empty them when the procedure is finished. This can be a conceivable safety issue since one needs to keep several liters of acid stored in the heat exchanger all the time when people is present in the etching area.

For this reason, the fundamental goal of this particular simulation was to demonstrate the possibility of maintaining the acid temperature inside the cavity below 15 C while using only the cooling water as heat exchange media. In order to simulate this condition, an hypothesis of free acid circulation throughout the cavity during the etching process had to be introduced.

The simplest way to numerically define the concept of free circulation would be to impose convective flux both at the inlet and outlet of the cavity. In this case though the system would not be constrained enough being all the boundaries described by Neumann conditions. In order to avoid the issue it was decided to change the inlet boundary to a Dirichlet condition where the value of temperature is fixed to be the same as the one at the outlet of the cavity in the previous step. This technique can be implemented in Comsol using boundary coupling variables.

This simulation was solved only in time dependent domain for up to 5400 seconds (*Figure 5.18*), roughly a full BCP process of 150 μm , to check the average temperature behavior of the acid in time. Initially the cooling water presented the same equilibrium temperature as the acid (15 °C) and during the process was lowered to less than 10 C. As a result the acid temperature monotonically decreased through the whole process demonstrating that enough cooling could be provided by the water with no need of adding an acid heat exchanger.

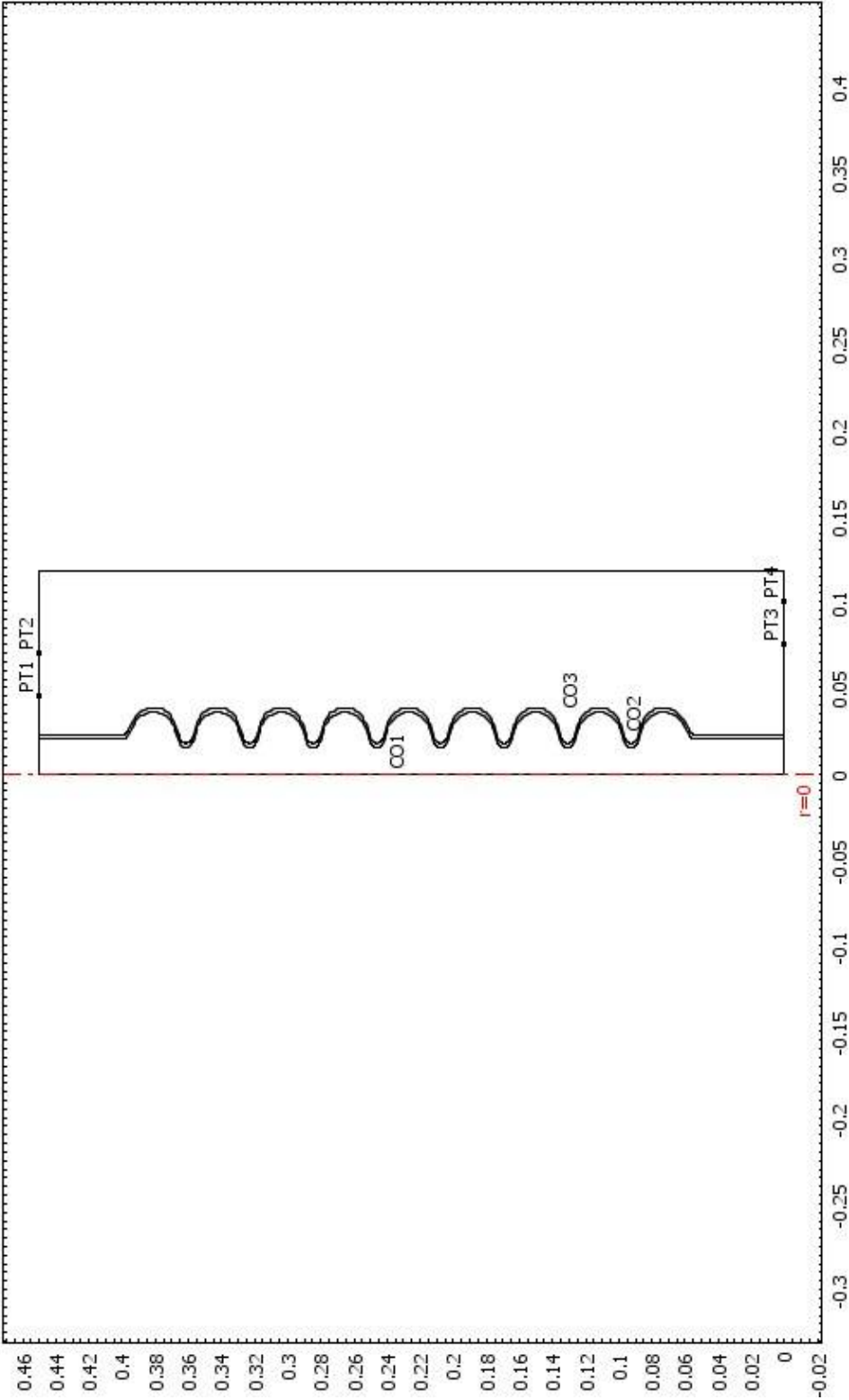


Fig. 5.1 BCP Facility: geometrical simplification

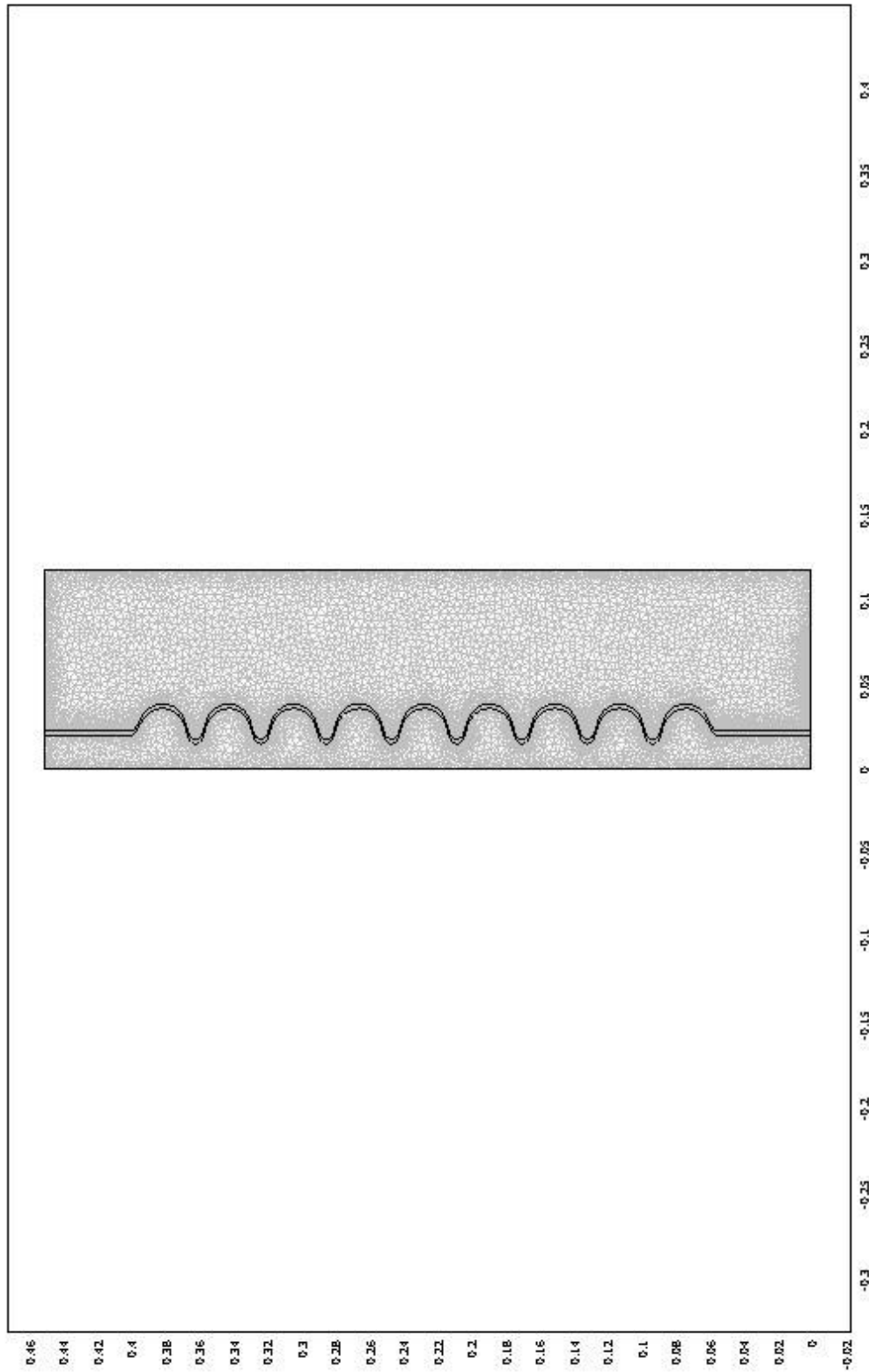


Fig 5.2 Triangular elements mesh

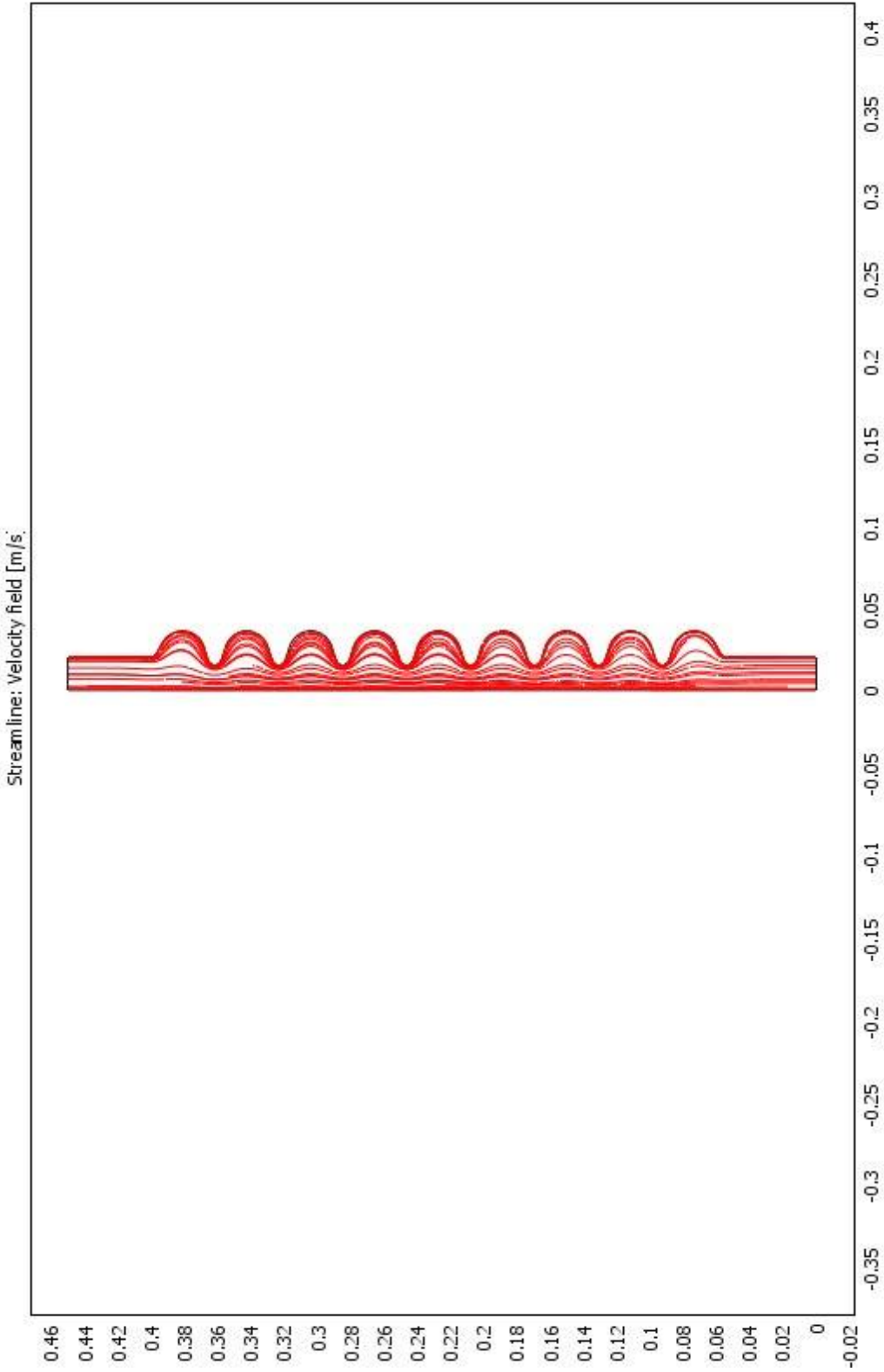


Fig. 5.3 Acid flow throughout the cavity: k-ε study

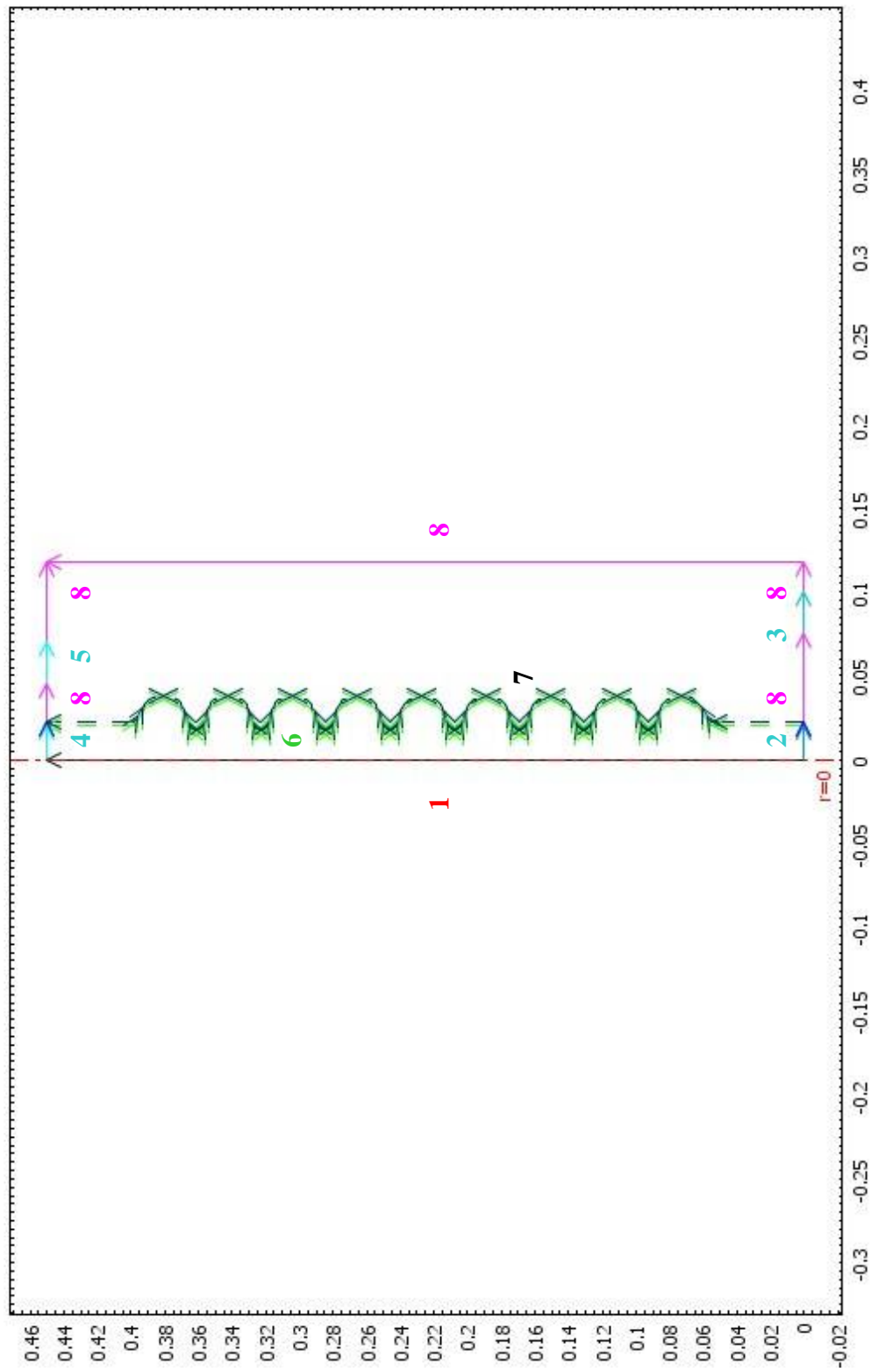


Fig. 5.4 Boundary conditions (resume)

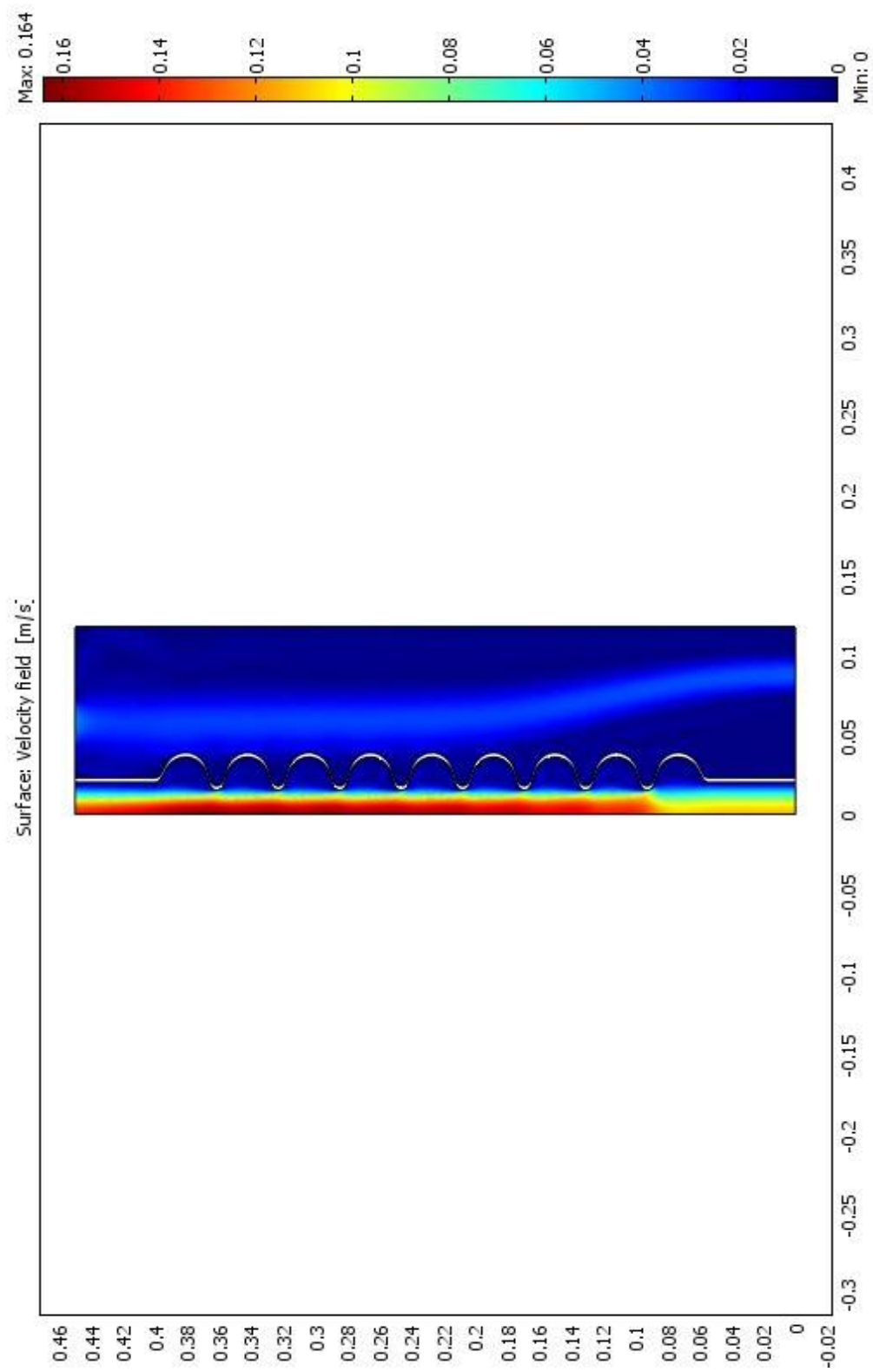


Fig 5.5 Facility 1. Velocity field map

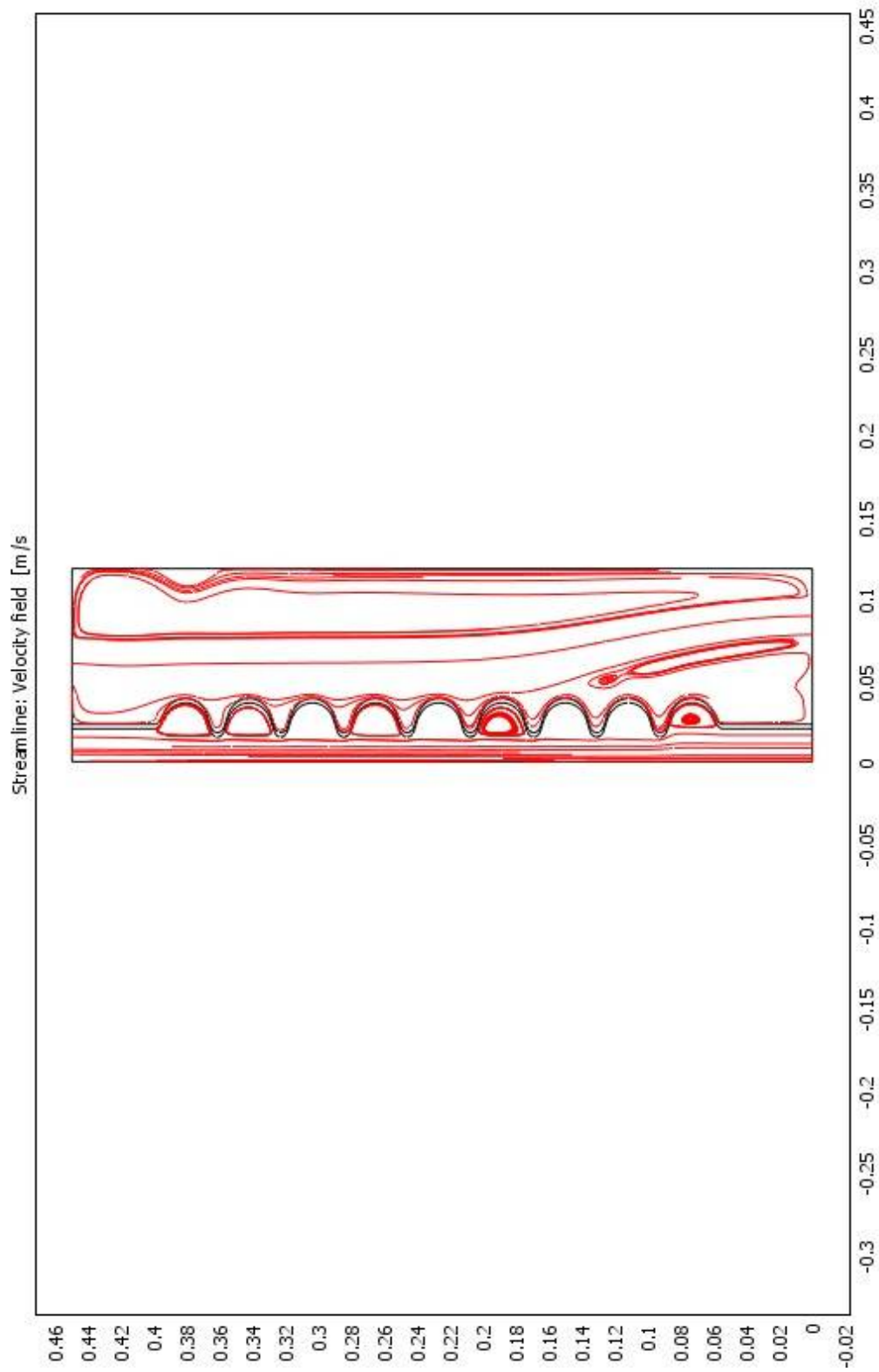


Fig. 5.6 Facility 1 Velocity field (steam line representation)

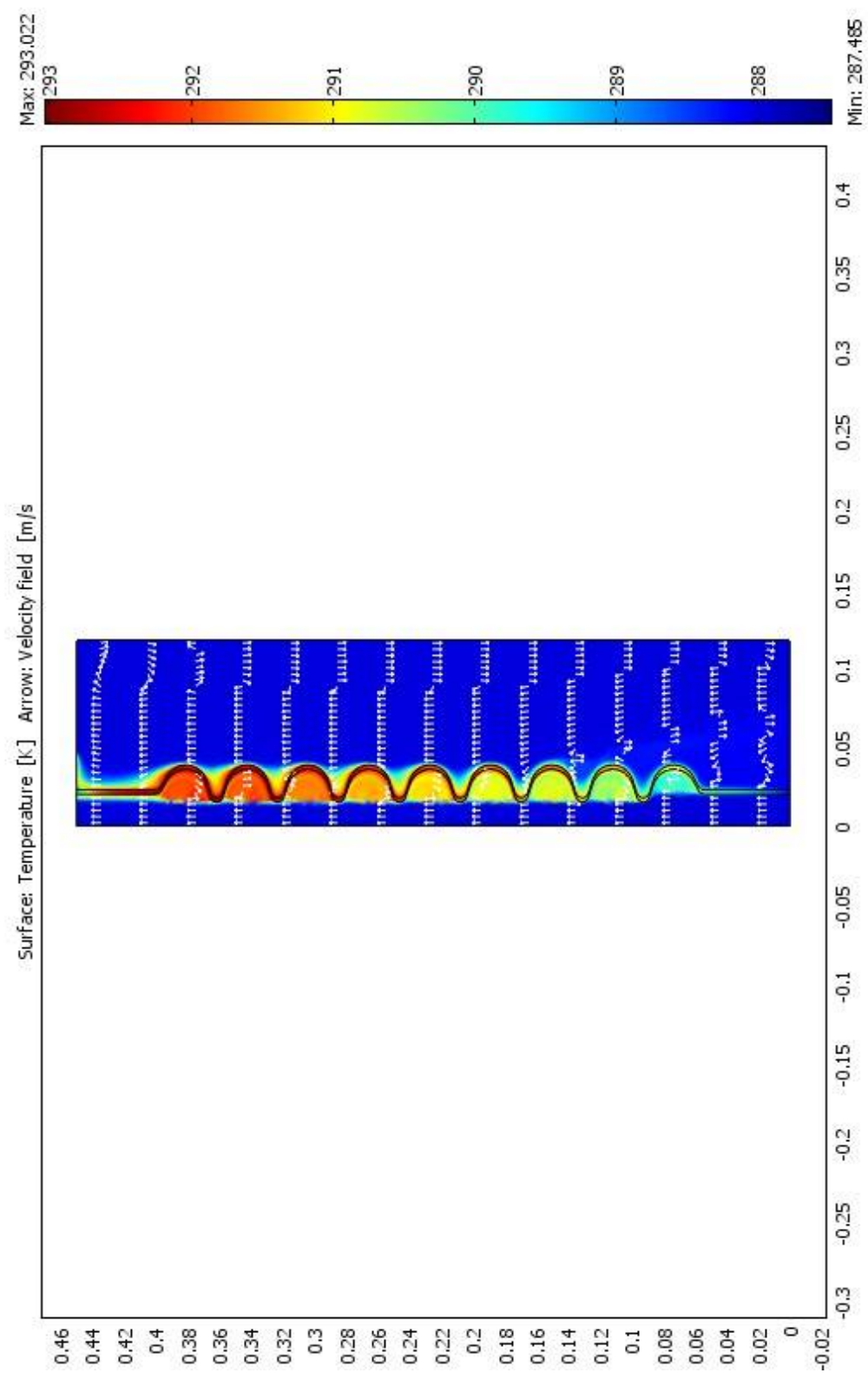


Fig 5.7 Facility 1 Temperature map

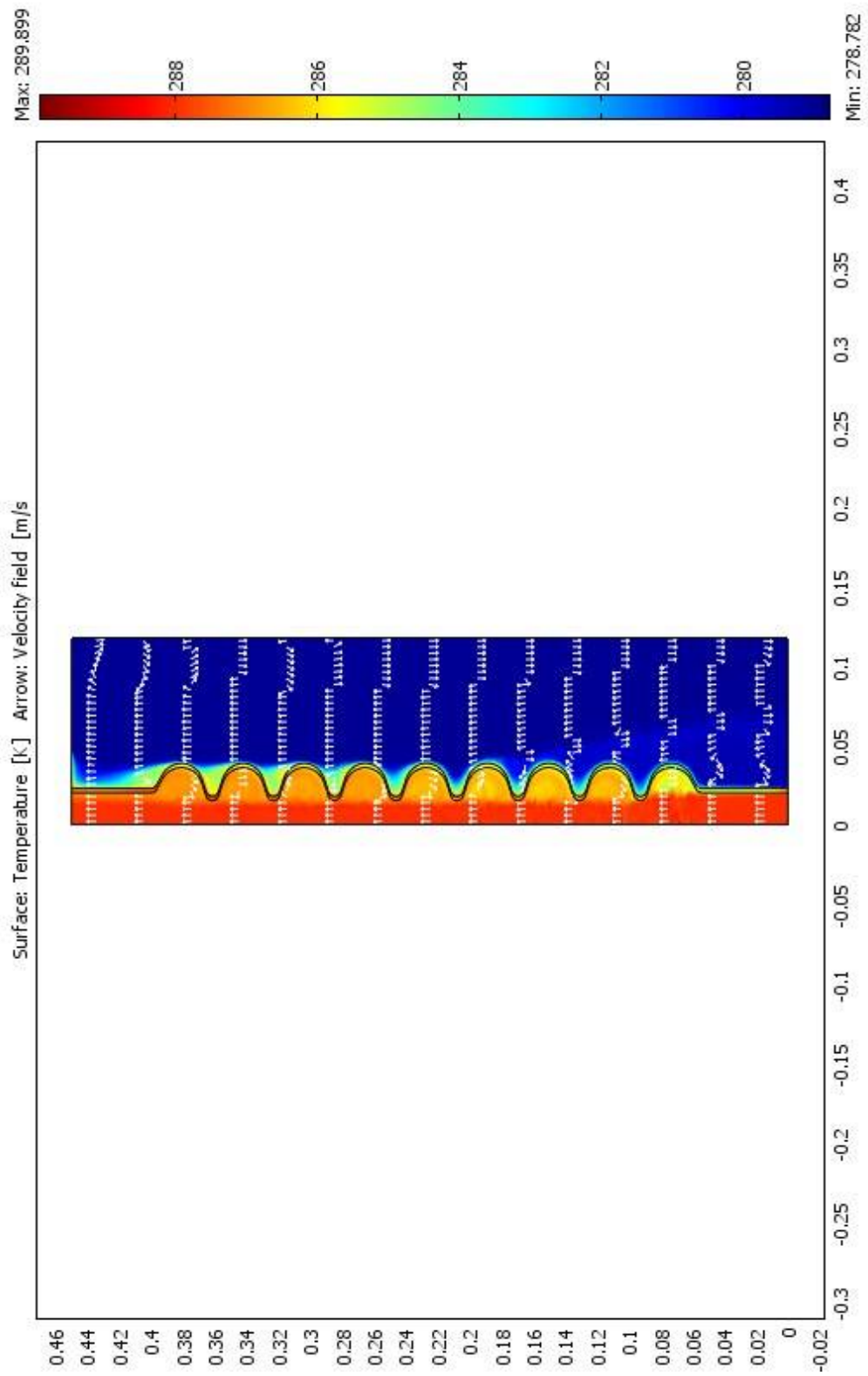


Fig 5.8 Facility 2 Temperature map

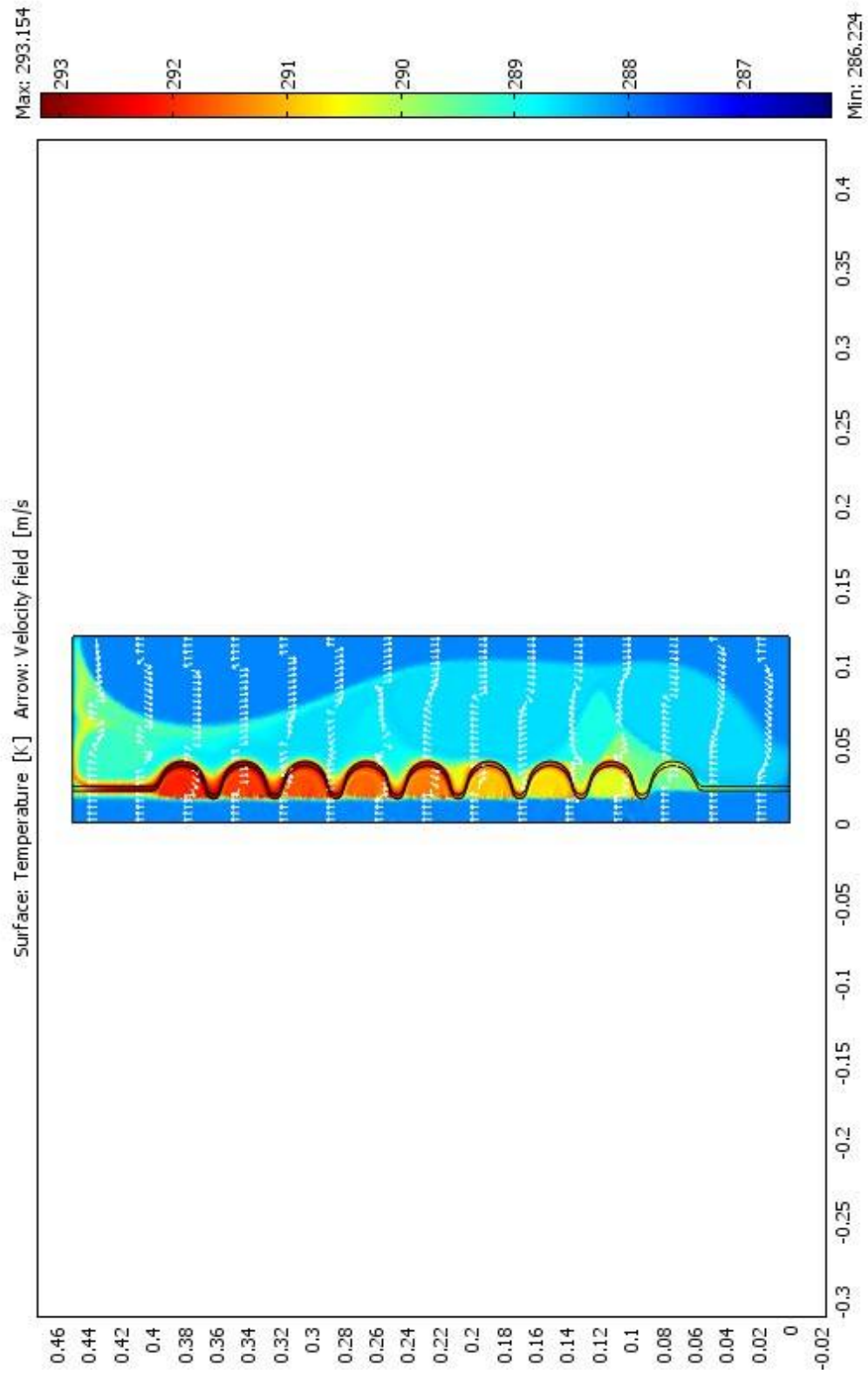


Fig 5.9 Facility 1. Acid-water counter flow. Temperature map

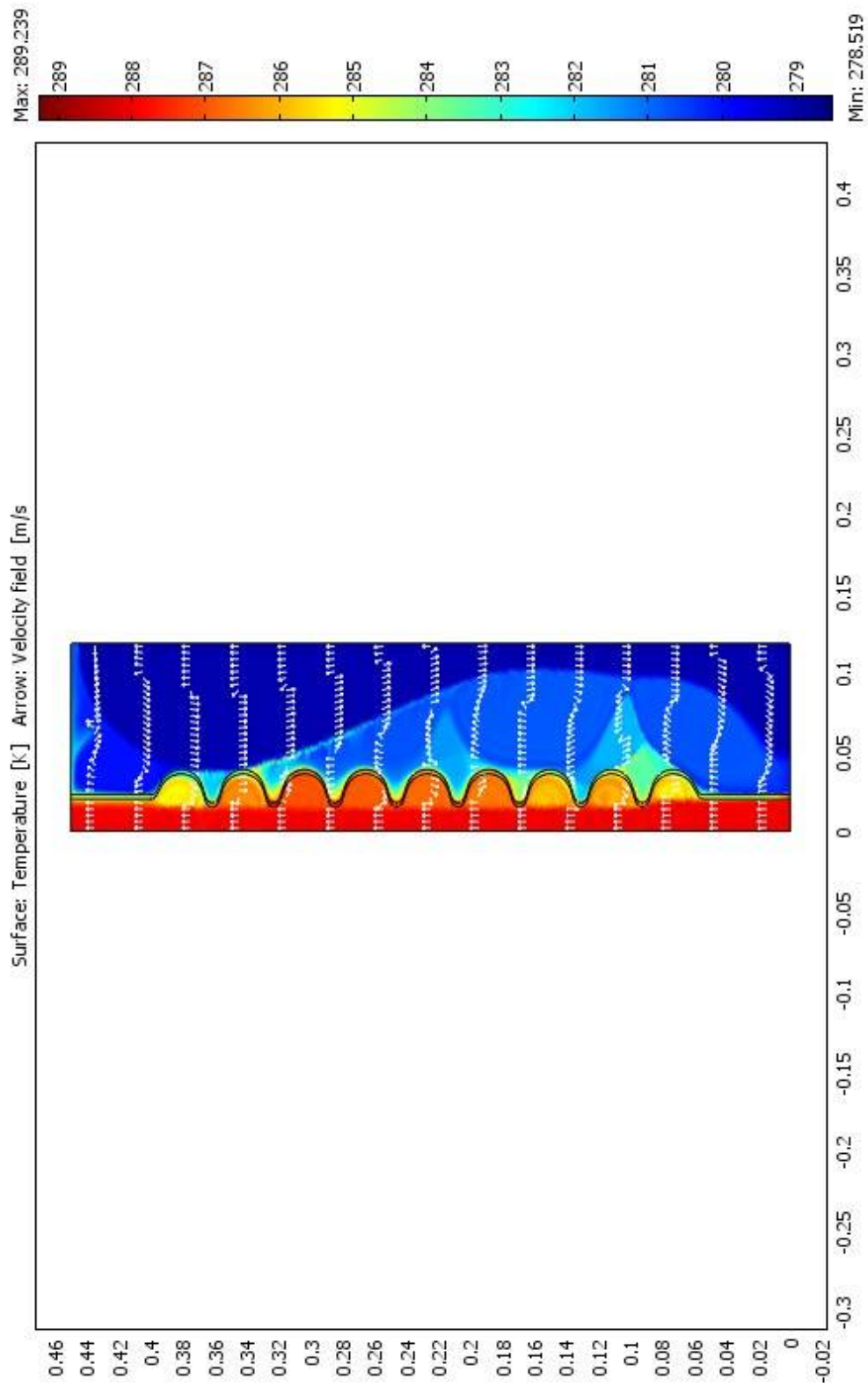


Fig 5.10 Facility 2. Acid-Water counter flow: Temperature map

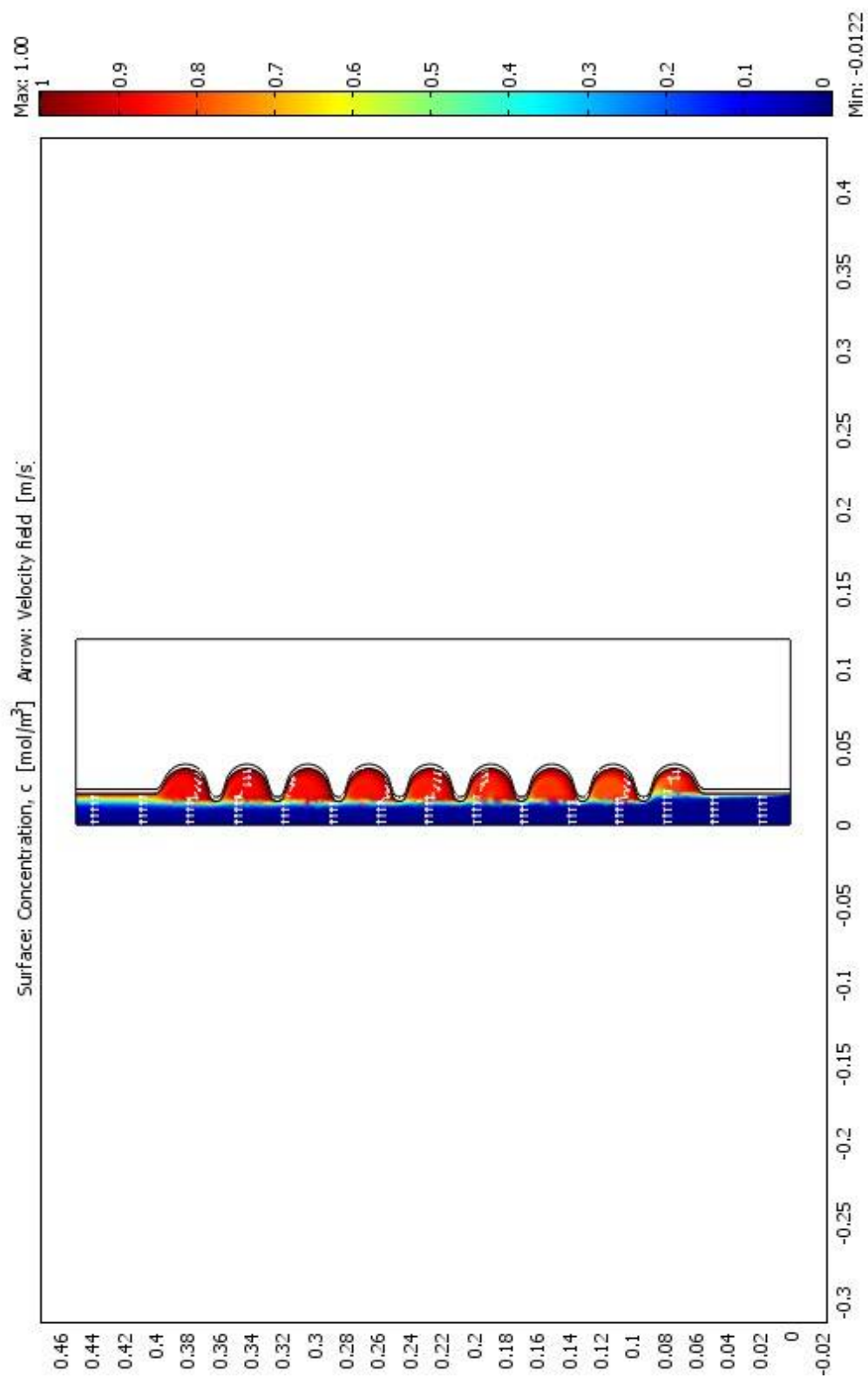


Fig. 5.11 Facility 1:Concentration of Niobium map.($D=10^{-7}$ m²/s)

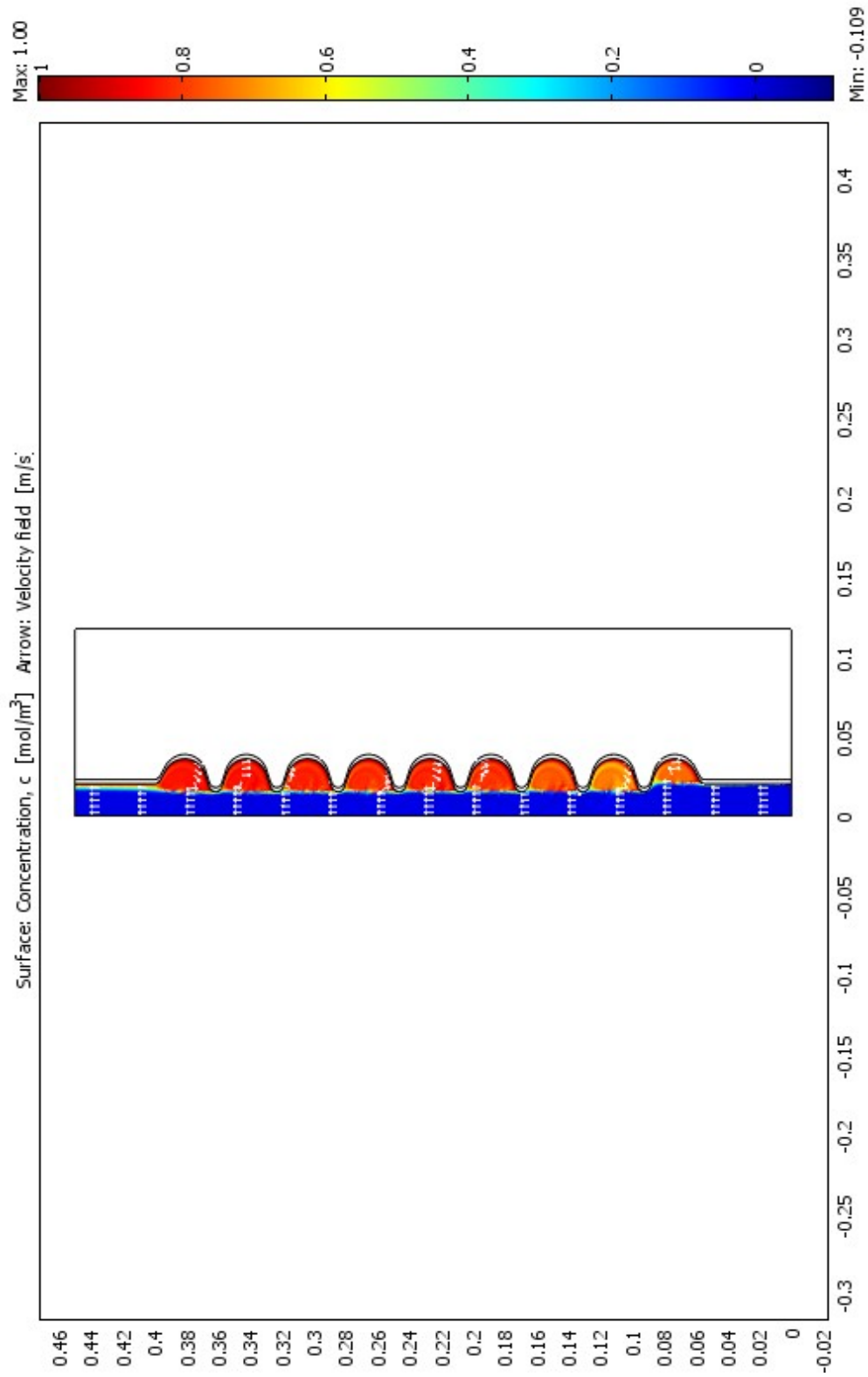


Fig. 5.12 Facility 1: Concentration of Niobium map.($D=10^{-8}$ m²/s)

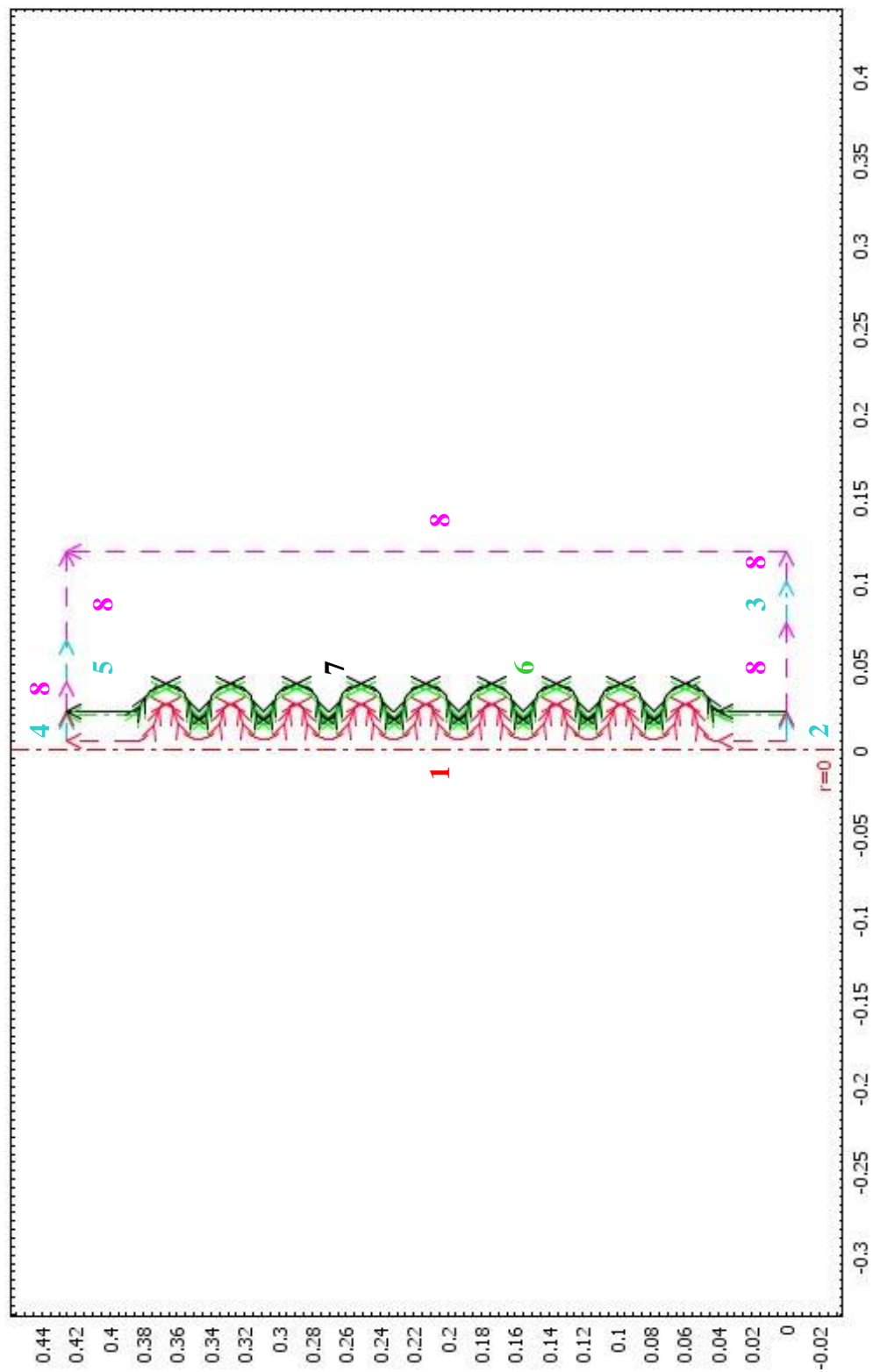


Fig. 5.13 Balloon system evaluation. Boundary conditions (resume)

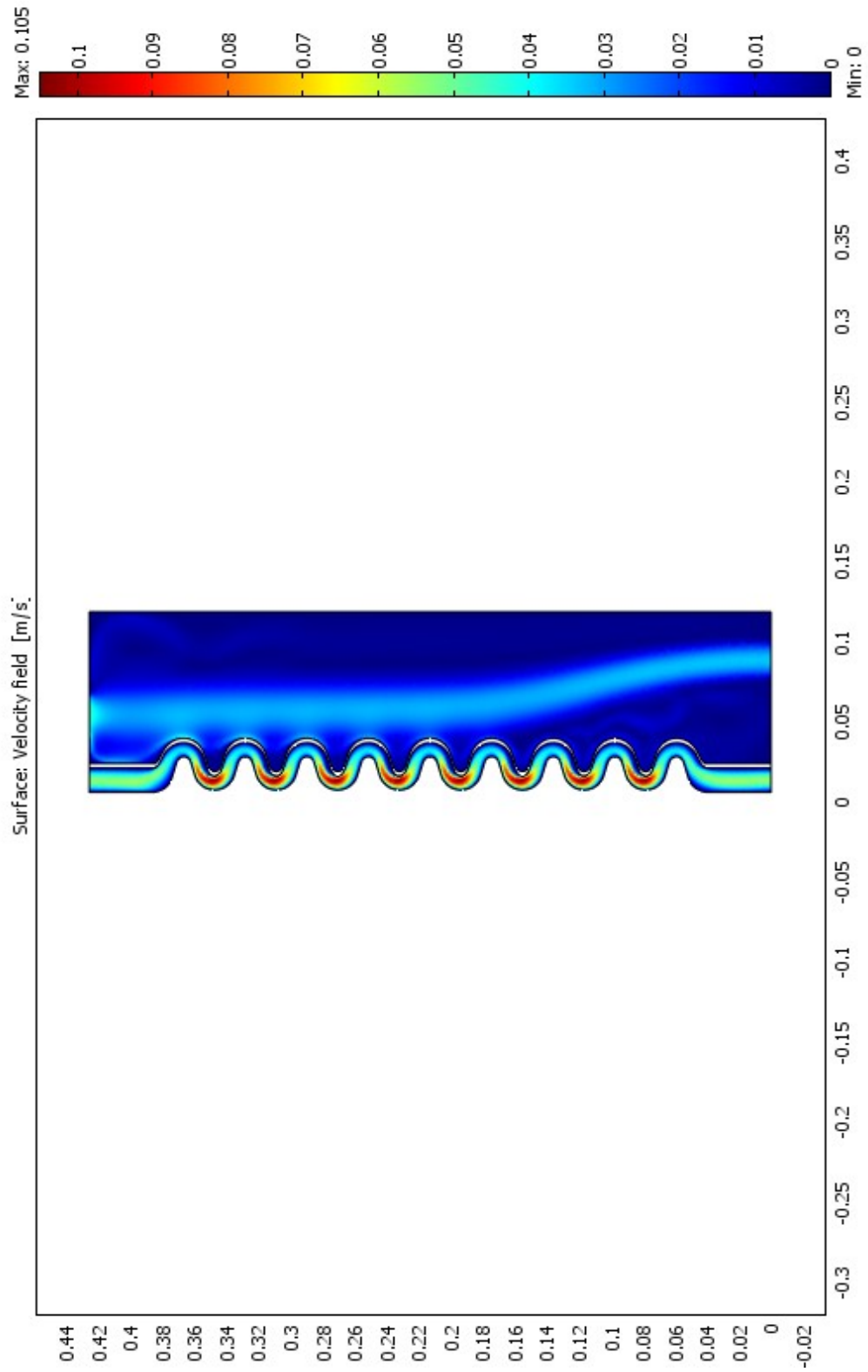


Fig 5.14 Balloon system evaluation. Facility 2 velocity field map

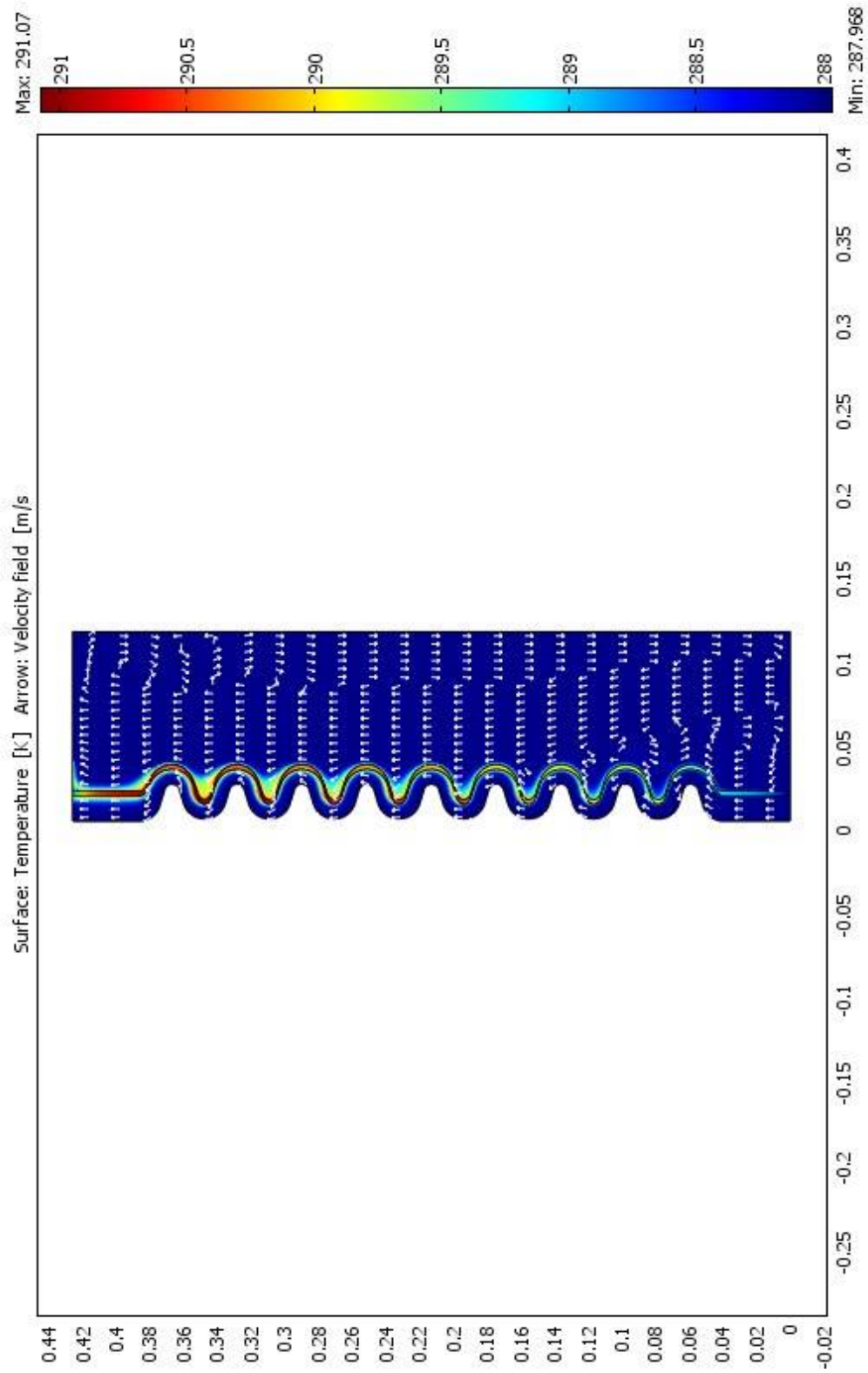


Fig 5.15 Balloon system envalutation.Facility 1: Temperature map

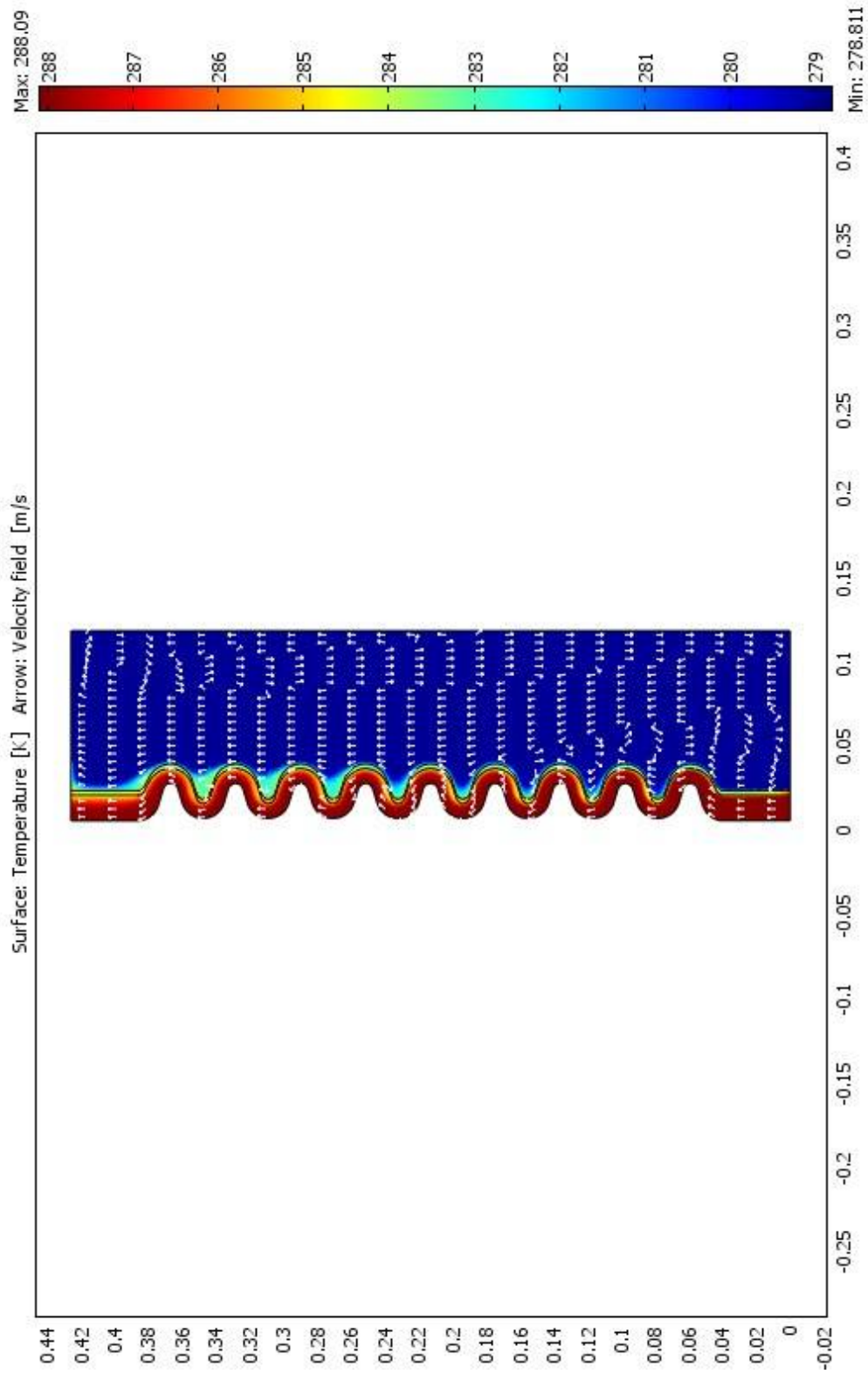


Fig 5.16 Balloon system envallutatio.Facility 2: Temperature map

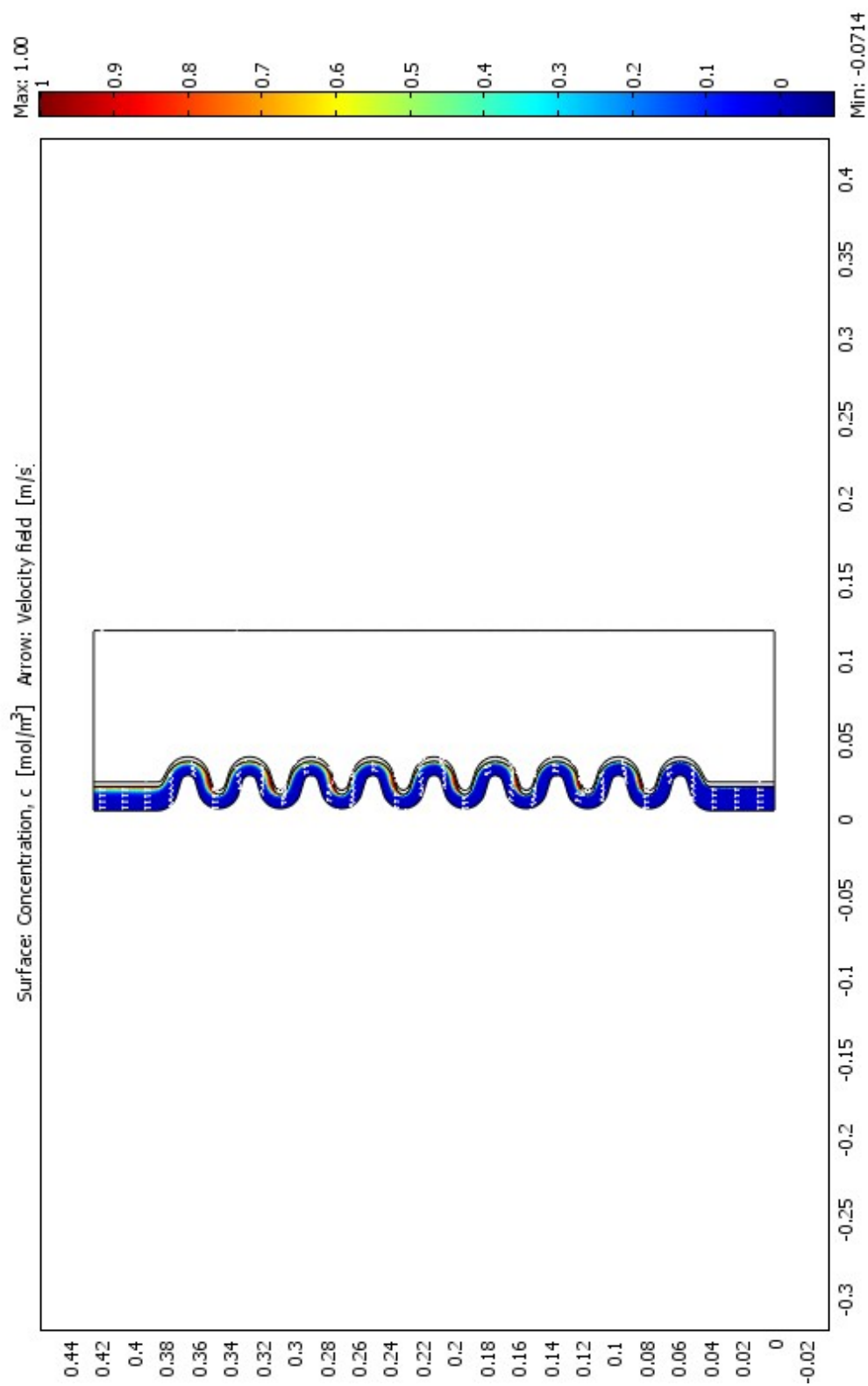


Fig 5.17 Balloon system evaluation. Facility 1: Concentration of Niobium map

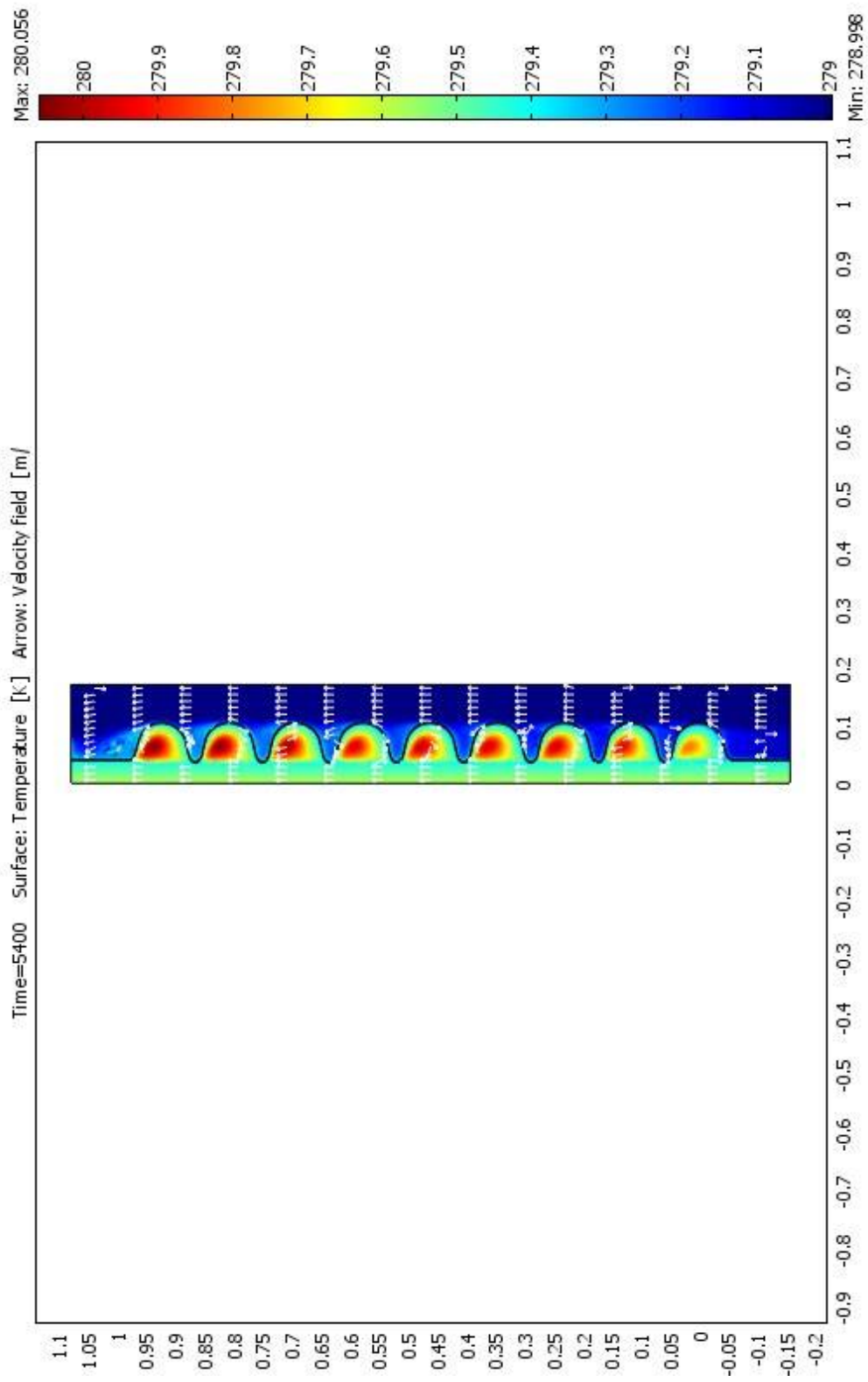


Fig. 5.18 Cavity 1.3 GHz Facility: Temperature map after 5400sec

CONCLUSIONS

The initial goal of this work was to evaluate the possibility to solve the differential etching issue that appear when the BCP process is employed during the production of the Fermilab 3.9 GHz 9-cell niobium cavities which are a key component of the future DESY XEFL and possibly of the ILC injection system. These simulations, limited in accuracy by not taking into consideration the acid speed and temperature dependence with respect to the etching rate, are consistent with experimental observations of the BCP process. In particular they confirm the limited cell circulation as the main factor influencing the differential etching between iris and equator. In addition they demonstrate that increasing the water-cooling system capacity helps optimizing the cell to cell temperature distribution.

These results are also consistent with bench-top experiments performed at Fermilab demonstrating that for this type of cavity, given their acid volume to Niobium surface ratio, the reaction rate slows down and eventually stops after 30 minutes if the acid is not properly circulated.

In order to improve the process, several simulations were performed with the goal of evaluating the impact on flow and temperature of a flow diverter inserted in the cavity. Installing a simple baffle with dimensions smaller than the iris is not very effective due to the acid high viscosity. In order to avoid this phenomenon it was decided to adopt a flow diverter with optimized shape and dimensions in order to equalize the material removal between the iris end equator. Hence a system of nine PET balloons has been inserted inside the cavity in order to avoid the acid stagnation inside the cells and guarantee an uniform material removal.

The simulations have demonstrated that the balloons option is very effective and should be pursued further.

The same type of simulations was also used in the preliminary study of the new simpler Facility for realize the 1.3 GHz cavities BCP.

The present work can be considered a starting point for futures studies and investigations. For example the temperature dependence of the acid viscosity should be implemented as well as the diffusion of niobium in solution to fully characterize the chemical reactions.

BIBLIOGRAPHY

- [1] TESLA - *Technical Design Report*, Part I, Executive summary 2001
- [2] Discovering the quantum universe, report 2006
<http://interactions.org/quantumuniverse/qu2006/index.html>
- [3] G.Comini, G.Cortella, *Fondamenti di trasmissione del calore*, Servizi Grafici Editoriali, Padova, 2001
- [4] O.C. Zienkiewicz, R.L. Taylor, *The finite element method (Vol.3 Fluid dynamics) Fifth edition*, Bulterworth-Heinemann editions, 2000
- [5] Quin Xue, *Modelling and simulation of the chemical etching process in niobium cavities*, Thesis work, Taiyuan University of Thecnology, 1995
- [6] W. D. Moeller et al., *HOM Couplers Issues for the 3.9 GHz cavity*, Presentation at the TTC meeting in KEK, Japan September 2006
- [7] B. Visentin et al., *Cavity baking: a cure for the high accelerator field Q-drop*, workshop on RF superconductivity, 1999
- [8] P. Bauer et al., *Evidence for Non-Linear BCS Resistance in SRF Cavities*, SRF workshop, 2005
- [9] TTF Collaboration, *Superconducting TESLA cavities*, physical review special topics-accelerators and beams, volume 3. 2000.
- [10] P. bauer et al., *Recent RRR measurements on Niobium for Superconducting RF Cavities at Fermilab*, SRF workshop, 2005
- [11] Lutz Lilje: *Experimental Investigations on Superconducting Niobium Cavities at Highest Radiofrequency*, Fields Dissertation zur Erlangung des Doktorgrades des Fachbereichs Physik der Universitaet Hamburg, Hamburg 2001
- [12] T. Higuchi, *Hydrogen adsorption in EP of niobium*, Hydrogen workshop, 2002
- [13] T. Saeky et al., *Latest results of high gradient cavities at KEK*, SMTF collaboration meeting, 2005
- [14] D. Bloess et al.. *Preparation and Handling of Surfaces for Superconducting RF Cavities*, workshop on RF superconductivity, 1988
- [15] P. Kneisel, *Latest Developments in Superconducting RF Structures*, EPAC 2006
- [16] P. Kneisel, *Update on lare grain and single crystal cavities*, TTC collaboration meeting, 2006
- [17] C. Boffo et al., *Facility for Chemical Polishing of Superconducting Niobium RF Cavities*, Advances in Superconductivity Conference, 2004
- [18] C. Boffo et al., *PH and Resistivity of the BCP Mix Diluted in UPW*, Fermilab internal note TM-2233, 2004
- [19] C. Boffo et al., *Control System for the BCP Facility at Fermilab*, SRF workshop, 2003
- [20] C. Boffo et at., *Optimization of the BCP processing of elliptical SRF cavities*, EPAC 2006
- [21]S.-J. Lee, J.-J. Lai & Y.-T Lin, *Simulation of the formation mechanism of a viscous layer for the electropolishing process*, Department of Mechanical Engineering, Yuan Ze University, Taiwan WIT Transactions on Engineering Sciences, Vol 48, 2005 WIT